Dissertation

F6

Faculty of Transportation Sciences
Department of Mechanics and Materials

Strain-rate sensitive cellular materials for energy absorption

Ing. Tomáš Doktor

Supervisor: prof. Ing. Ondřej Jiroušek, Ph.D.
Supervisor–specialist: doc. Ing. Daniel Kytýř, Ph.D.
Study programme: Technology and Technics of Transport and Communications
Field of study: Transportation Systems and Technology
October 2020

Acknowledgements

I would like to thank my supervisors prof. Ing. Ondřej Jiroušek, Ph.D. and doc. Ing. Daniel Kytýř, Ph.D., for the patient guidance and encouragement during my work.

I was delighted to cooperate with Ing. Ivan Jandejsek, Ph.D. during microfocus X-ray tomography, with MDDr. Eva Kamenická, an excellent operator of the micro-lathe and with Mgr. Veronika Koudelková, an expert in scanning electron microscopy.

I am really grateful for the fruitful cooperation with my dear friends and colleagues from Laboratory for impact and high strain-rate testing of materials and structures at CTU FTS and Department of biomechanics at ITAM AS CR, v.v.i., Ing. Petr Zlámal, Ph.D., Ing. Tomáš Fíla, Ph.D. and Ing. Petr Koudelka, who provided me useful advice and help and made our lab a pleasant and inspiring place to work at.

This work was supported by CTU in Prague (research projects No. SGS12/205/OHK2/3T/16 and SGS15/225/OHK2/3T/16), Czech Science Foundation (research projects No. P105/12/0824, 15-15480S and 19-23675S) and OPRDE project Engineering applications of Microworld Physics (reg. No. CZ.02.1.01/0.0/0.0/16_019/0000766). All the support is gratefully acknowledged.

Declaration

I hereby declare, that I wrote this thesis independently, under supervision of my supervisors, and I have cited all the sources used in accordance with the CTU guideline No. 2009/01 "On ethical preparation of university final theses".

Where indicated, description of the experimental campaigns and their results were published in peer-reviewed research papers, which I authored or co-authored. The copyright issues in such cases have been resolved.

Tomáš Doktor, *m. p.*
In Lysá nad Labem, 31 October 2020

Abstract

The aim of the dissertation was the investigation of the mechanical behaviour of cellular materials with an emphasis on lattices at higher strain-rates and possible enhancement of their energy absorption capabilities. Two types of cellular materials and lattices were test, closed- and open-cell aluminium foam and SLS printed auxetics. To induce a strain-rate sensitive response in open-cell structures (foams and lattices), different types of polymeric fillers were tested (polyurethane putty, polyurethane foam and ordnance gelatin) to form Interpenetrating-phase composites (IPCs)

A multi-level mechanical testing was carried out to assess the mechanical properties of both the base material and cellular structure. At the micro-scale level, the experiments were performed using an in-house testing apparatus in conjunction with the optical strain measurement using Digital Image Correlation. At the macro-level, for the investigation of the cellular structure a time-lapse X-ray tomography of the compression test was performed.

For the testing of the mechanical response under impacts, two types of tests were used to cover a broader range of strain-rates: (i) drop tests and (ii) Split Hopkinson pressure bar (SHPB). The experimental campaigns carried out at moderate strain-rates using a drop tower showed a strain-rate sensitive response at moderate strain-rates in the ordnance gelatin and IPC, while the response of unfilled aluminium foam remained unchanged with an increasing strain-rate. The high strain-rate impact using the SHPB showed a strain-rate sensitivity in the impact energy absorption characteristics (plateau stress, strain energy density) for all the tested materials (polyurethane foam, ordnance gelatin, polyurethane putty, IPC). The high strain-rate impact tests confirmed the positive influence of both types of tested filling (polyurethane foam, ordnance gelatin) on energy absorption capabilities of the additively manufactured auxetics. The optical strain measurement of the SHPB impact tests of the polymer-filled auxetics showed a reduction in the auxetic nature with the presence of the filling.

Keywords: impact energy absorption, strain-rate sensitivity, cellular materials, inter-penetrating phase composites

Supervisor: prof. Ing. Ondřej Jiroušek, Ph.D.

Abstrakt

Disertační práce se zabývá měřením mechanické odezvy porézních kovových materiálů (pěn a periodických stuktur) za vysokých rychlostí deformace a možnostmi zvýšení schopnosti pohlcení nárazové energie pomocí polymerní výplně. Byly testovány tři typy porézních kovových materiálů (kovová pěna s uzavřenými a otevřenými póry a auxetické struktury vyrobené technologií SLS). Pro získání odezvy citlivé na rychlost deformace byly testovány tři zástupci polymerních materiálů: neporézní a porézní polyuretan a balistická želatina.

Na mikroúrovni byly provedeny ohybové testy stěn buněk kovové pěny pomocí vlastního zatěžovacího zařízení. Deformace byly měřeny opticky metodou digitální korelace obrazu. Na makroúrovni byla pro sledování deformací uvnitř buněčné struktury využita časosběrná rentgenová tomografie jednoosého tlakového testu.

Pro stanovení odezvy testovaných materiálů na nárazové zatížení bylo využito padostroje a dělené Hopkinsonovovy tyče (SHPB) pro pokrytí širokého rozsahu rychlostí. Za nižších rychlostí deformace při testech v padostroji bylo zjištěno zvýšení hustoty deformační energie při testech vyplněné kovové pěny a balistické želatiny, zatímco nevyplněná kovová pěna změnu nevykazovala. Testy v SHPB potvrdily zvýšení hustoty deformační energie pro všechny testované výplně i pro vyplněnou kovovou pěnu a auxetické struktury. Pomocí optického měření deformací byl pozorována redukce auxetického chování u vyplněných auxetických struktur.

Klíčová slova: pohlcování nárazové energie, rychlost deformace, porézní materiály, kovové pěny

Překlad názvu: Materiály s odezvou citlivou na rychlost deformace pro pohlcování nárazové energie

Contents

1 Introduction **1**
1.1 Motivation 1
1.2 Aims and objectives 2
1.3 Thesis structure 3

2 The State of the Art **5**
2.1 Materials 5
2.1.1 Cellular solids 6
2.1.2 Meta-materials 8
2.1.3 Inter-penetrating phase composites 9
2.1.4 Auxetics 10
2.2 Multi-level characterisation of cellular materials 11
2.2.1 Properties of base material: micro-mechanical testing 12
2.2.2 Optical strain measurement 13
2.2.3 Time-lapse tomography . . 13
2.2.4 Inverse estimation of material model parameters using finite element analysis 15
2.3 Dynamic testing 16
2.3.1 Moderate strain-rate impacts testing 16
2.3.2 High strain-rate impact testing 17
2.4 Summary 19

3 Structural properties and quasi-static mechanical response **21**
3.1 Investigated materials 22
3.1.1 Cellular metals 22
3.1.2 Filling materials 22
3.1.3 IPC 23
3.2 Time-lapse tomography of compression test 23
3.2.1 Specimen preparation 23
3.2.2 Loading procedure 24
3.2.3 X-ray imaging 25
3.2.4 Digital volumetric correlation 25
3.2.5 Results 26
3.2.6 Concluding remarks 26
3.3 Micro-scale loading tests 27
3.3.1 Specimen preparation 27
3.3.2 Loading device 30
3.3.3 Strain measurement 31
3.3.4 Inverse finite element analysis 33
3.3.5 Results 35
3.3.6 Concluding remarks 36
3.4 Macroscopic quasi-static tests 37
3.4.1 Specimen preparation 38
3.4.2 Testing procedure 39
3.4.3 Results 40
3.4.4 Concluding remarks 41
3.5 Summary 42

4 Moderate strain-rate impact testing **43**
4.1 Experimental methods: Drop test 43
4.1.1 Impact test procedure . . . 43
4.1.2 Instrumentation 44
4.1.3 Stress and strain measurements 45
4.2 Results 46
4.3 Concluding remarks 49

5 High strain-rate impact testing **51**
5.1 Specimen preparation 51
5.2 SHPB tests 52

5.3 Results 53
5.4 Concluding remarks 58

6 Auxetic structures: towards higher impact energy absorption 59

6.1 Effect of joint stiffness 59
6.1.1 Specimen design and manufacturing 60
6.1.2 Compression tests 61
6.1.3 Results 63
6.1.4 Concluding remarks 64
6.2 Effect of filling 65
6.2.1 Specimens' design and manufacturing 65
6.2.2 Quasi-static tests 67
6.2.3 SHPB tests 67
6.2.4 Evaluation 68
6.2.5 Results 68
6.2.6 Concluding remarks 72

7 Summary 73

Bibliography 75

A Candidate's publications related to the dissertation 87

Papers published in journals with impact factor 87
Proceedings papers listed by Scopus and/or Web of Science 88
Candidate's publication and citation metrics 88

Figures

2.1 Stress-strain curve of energy absorber 6
2.2 Classification of metal foam production techniques 7
2.3 Production scheme of the Alporas aluminium foam 8
2.4 Investment casting process . . . 8
2.5 Principle of microtomography 14
2.6 Principle of Digital Volumetric Correlation 15
2.7 Scheme of Kolsky setup (SHPB) 17

3.1 Experimental setup for the time-lapse tomography of the compression test 24
3.2 Visualisation of the reconstructed CT image 25
3.3 Results of the DVC on the image data acquired by the time-lapse tomography 27
3.4 Single-wall specimens used in the micromechanical experiments (three point bending): Projections of the cell-wall specimen 29
3.5 Original three-point bending experimental setup developed for testing of the human trabeculae 30
3.6 Improved design of the supports for the three-point bending tests 31
3.7 Loading setup for the cantilever bending test. 31
3.8 Detailed image of the tested specimen placed in the loading device 32
3.9 Displacement paths 33
3.10 Example of the tetrahedral mesh of the isolated cell-wall tested in the three-point bending 34
3.11 Example of the numerical results from the FE simulation of the three-point bending test: vertical displacements 34
3.12 Results of the inverse FE simulation of the micro-scale three-point bending test 36
3.13 Experimental results of the cantilever bending tests 37
3.14 Specimen of the AL003860 open-cell foam. The scale bars correspond to 10 mm 38
3.15 Experimental setup used for quasi-static tests. 40
3.16 Stress-strain curves of the representatives of filling materials. 41

4.1 Drop tower developed at CTU FTS 45
4.2 Results of the moderate strain-rate impact tests of the ordnance gelatin. 47
4.3 Loading scene of the selected sample (group A3) in several loading steps (the time step between the captured images is 0.89ms). 47
4.4 Results of the moderate strain-rate impact tests of the open cell aluminium foam. 48

4.5 Results of the moderate strain-rate impact tests of the IPC. 49

5.1 SHPB setup. 53
5.2 Example of the force equilibrium diagram for the polyurethane putty specimen tested at 1.5 bar. 54
5.3 Results of the SHPB impact tests of the polyurethane foam. 54
5.4 Results of the SHPB impact tests of the ordnance gelatin. . . 55
5.5 Results of the SHPB impact tests of the polyurethane putty. 56
5.6 Results of the SHPB impact tests of the IPC. 56
5.7 Comparison of the intact and deformed state of the filling materials' specimens under impact loading. 57

6.1 Geometry of the used auxetic unit cell. 61
6.2 STL models for 3d printing. . 62
6.3 Loading scene with tracking features and tracked displacement paths 62
6.4 Stress-strain curves of the 3D re-entrant specimens with the different reinforcement in the struts' joints. 63
6.5 Samples of the auxetics tested with fillings 66
6.6 Results of the SHPB impact tests of the 2D re-entrant structure - comparison of the filled and unfilled samples 68
6.7 Results of the SHPB impact tests of the 3D re-entrant structure - comparison of the filled and unfilled samples 69
6.8 Results of the SHPB impact tests of the 2D missing rib structure - comparison of the filled and unfilled samples 69
6.9 Poisson's function measured in the group of 2D re-entrant specimens. 71
6.10 Poisson's function measured in the group of 3D re-entrant specimens. 71
6.11 Poisson's function measured in the group of missing rib specimens. 72

Tables

3.1 Overall mechanical and structural properties Alporas and AL003860 22
3.2 Results of the inverse FE simulation of the micro-scale three-point bending test 36

4.1 Impact test parameters - testing of the ordnance gelatin. 44
4.2 Impact test parameters - testing of the cellular metal and IPC . . 45
4.3 Impact test results - bulk ordnance gelatin. 46
4.4 Comparison of the strain energy density up to 21% deformation 49

6.1 Design parameters - common parameters. 60
6.2 Design parameters - joint reinforcement variations. 61
6.3 Average results in the tested groups. The stress and strain at the first collapse. Average Poisson's number. 64
6.4 Mechanical properties of the base material for the SLS (316L-0407 alloy) 66
6.5 Density of the polymer-filled auxetics 67
6.6 Comparison of the plateau stress and strain energy density for the filled auxetic samples 70

Chapter 1

Introduction

1.1 Motivation

An impact energy absorption capability is a widely required feature in safety applications, where mitigation of possible damage to humans or critical parts of infrastructure is desired.

The mitigation of passenger injuries in the automotive field (also known as passive safety) has attracted attention for many decades [1] and is still considered among the most important tasks in this field [2, 3]. According to the World Health Organization report on road traffic injury prevention [4], vehicle safety standards posed the largest contribution to a reduction in road crash casualties.

Aside the automotive field, improvements in impact energy absorption capabilities pose innovations in other fields, e.g. blast-protective panels with energy absorption layers [5, 6, 7]. Dependent on impact scenarios, which come into consideration (e.g. car crashes, bicycle or motorcycle accidents or blasts during e.g. industrial explosions or terrorist attacks), specific ranges of impact velocities and levels of impact energy are required to be absorbed.

Porous materials, especially cellular metals represent a promising group of impact energy absorbers. Such materials are currently well established mainly in damping and insulation applications. However, the utilisation of porous materials in a wider range of engineering applications belongs to the novel trend of bioinspired techniques, when humans try to follow nature in order to exploit the long evolution period. The usage of porous or cellular materials may be considered as the opposite to the efforts to achieve the highest homogeneity and purity of the materials used in technical applications [8]. The utilisation of

cellular metals in sophisticated engineering fields requires detailed knowledge of their physical properties, among which mechanical properties are of high importance for structural applications, usage in transportation as well as for biomedical applications. In impact energy absorption, the capabilities of the cellular metals may reach favourable enhancement by controlling the properties of the cellular structure. Moreover, the cellular structure or the lattice may be equipped with a filling material which enables the further control of the deformation response.

1.2 Aims and objectives

The aim of the dissertation is the investigation of the mechanical behaviour of cellular materials with an emphasis on lattices at higher strain-rates and possible enhancement of their energy absorption capabilities. The mechanical response of the tested materials was studied at different impact velocities in order to simulate their response under different impact scenarios. To induce a strain-rate sensitive response in open-cell structures (foams and lattices), different types of polymeric fillers were tested: (i) polyurethane putty, (ii) polyurethane foam and (iii) ordnance gelatin. The first two types of material represent solid and cellular polymers while the third one was selected due to its highly strain-rate sensitive nature which had been reported previously in literature [9].

Among the lattices, auxetics, a class of materials with a negative Poisson's ratio, have the potential to increase the impact resistance, especially under localised impacts. Therefore, one of the objectives of the thesis is the investigation of the fillers' influence on the impact response of auxetics.

Cellular metals exhibit heterogeneity at several scale levels. Aside the heterogeneous cellular structure, the solid material of the cell-walls is also heterogeneous due to presence of micropores or residuals of the foaming agents. Since cellular material may be considered both as a material and as a structure, this distinction for metal foams has to be selected in this study as well. Hence, the cells and cell-walls will be considered as structural elements of the porous structure, while the cell-walls themselves will be considered as homogeneous.

Based on the above mentioned assumptions, the materials were investigated at the level of the extracted cell-wall specimens, to describe the material

properties of the base material of the cellular metal, and at the structural level. At the structural level, the cellular structure was studied tomographicaly under a gradually increasing load. In further parts of the study (during the dynamic tests), the response of the investigated materials was studied at the macro-level.

1.3 Thesis structure

Chapter 1 defines aims and goals of the dissertation and specifies the tasks to achieve these goals.
Chapter 2 presents the state of the art materials and methods related to the objectives of the dissertation. The types of materials used as impact energy absorbers are presented, both widely-used ones and novel types. The principles of the main experimental techniques used in the study are also described in this chapter, focusing both on the well established methods and the in-house developed techniques.
Chapter 3 deals with the detailed description of the cellular structure of the metal foam using time-lapse computed tomography and with the investigation on the material properties of the base material of the metal foam by micro-scale mechanical tests. Moreover, this chapter introduces the description of the effective mechanical properties of cellular metals, filling materials and interpenetrating phase composites (IPCs) under quasi-static loading conditions.
Chapter 4 presents the experimental campaign focused on testing the cellular metals and IPCs under moderate strain-rate conditions. To achieve strain-rates in the range of dozens of s^{-1} testing in a drop tower was used.
Chapter 5 is focused on testing the mechanical response of the investigated filling materials and IPCs at higher strain-rates (range of thousands of s^{-1}) using split Hopkinson bar.
Chapter 6 describes two experimental campaigns, both dealing with investigations on the strain energy absorption of additively manufactured auxetics (structures exhibiting negative Poison's ratio). The first campaign deals with the influence of the controlled stiffness of the struts' joints in an auxetic lattice on the strain energy density and Poissions' functions. The second campaign is focused on the influence of the filling material on the impact energy absorption properties and on a proper description of the auxetic behaviour of the considered structures.

Chapter 7 summarises the results of the performed experimental campaigns, draws the conclusions and presents the utilisation of the results in the framework of broader research projects.

Chapter 2

The State of the Art

In this chapter, both the history and current research are presented for the (i) cellular materials used in the impact energy absorption applications and (ii) experimental techniques used for the characterisation of complex materials at different scale levels and different loading rates. The experimental setups and methods developed at the author's workplace and used in this thesis are presented here as well.

2.1 Materials

The materials used in impact energy absorption applications are expected to dissipate the kinetic energy of the impact into plastic deformation. A typical stress-strain curve which indicates the energy absorption properties is depicted in Figure 2.1. The loading diagram consists of three phases: (i) elastic region, (ii) plateau region and (iii) densification phase. The energy absorption capabilities are determined by the characteristics of the plateau region, i.e., by the values of the plateau stress and densification strain.

In most engineering materials, the response to mechanical loading varies with the different values in the rate of loading. This phenomenon, called strain-rate dependency or strain-rate sensitivity, was first observed in metals. However it is significant in many other groups of engineering materials, e.g., polymeric foams [11], aluminium foams [12, 13] or composites [14]. Considering the application point of view, strain-rate effects also play an important role in vehicle crashworthiness as the strain-rate hardening affects the impact energy dissipation during the crash [15, 16].

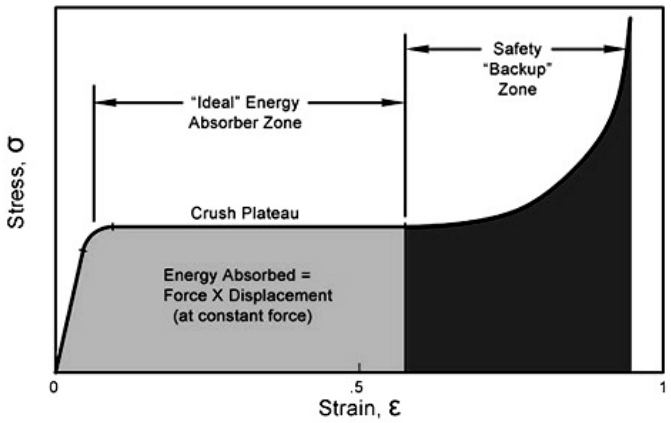

Figure 2.1: Stress-strain curve of an energy absorber [10]

2.1.1 Cellular solids

In natural porous material several functions may be identified, i.e., structural (carrying a weight), damping (change of kinetic mechanical energy), insulation (e.g. acoustic or thermal) or an increase in the reactive surface. The main advantages of porous structures are (aside their multifunctional capabilities) their high specific stiffness and strength. Among natural porous materials belong, for example, cancellous bone, corals, cuttlefish bone or honeycombs in which they all mainly have mainly structural (e.g., load bearing) functions, or lung or liver tissues, where the porous nature serves as an extension of the reactive surface [17]. Efforts to utilise the favourable properties of cellular materials in engineering started with the fabrication of artificial polymeric foams in the 1930's and 1940's. The first artificial foams were polymeric foams (polystyrene foam in 1931 and polyurethane foam at the beginning of WWII).

The first cellular metal was prepared in 1948 by Benjamin Sosnik [18]. In the foam prepared by Sosnik mercury was added as a blowing agent into the molten aluminium. In 1956, John C. Elliott invented a laboratory procedure for the production of a closed-cell metal foam, where mercury was replaced by blowing agents utilising thermal dissociation to produce gas [19].

In the 1980's a lot of attention was paid to the aluminium foam development in the Fraunhofer Institute in Bremen. In the early 1990's, Shinko Wire company in Japan started to produce aluminium alloy foams and made them commercially available under the brand name Alporas [8].

Currently, the majority of cellular metals produced originate from aluminium of aluminium alloys. There are efforts to utilise other metals as the base material for metal foams as well. However, for other metals, especially with higher melting points (e.g. titanium or iron with their melting points 1670 °C and 1530 °C, respectively) the foaming processes become more challenging.

During production, the pores are formed in different stages of the fabrication process, which determines the structural properties of the cellular architecture. Degischer, in [8], classified the techniques of cellular metal fabrication according to three criteria: (i) the metal condition during the pore forming process, (ii) the forming process and (iii) the method of pore formation. The classification of the production processes according to these criteria is listed in Figure 2.2.

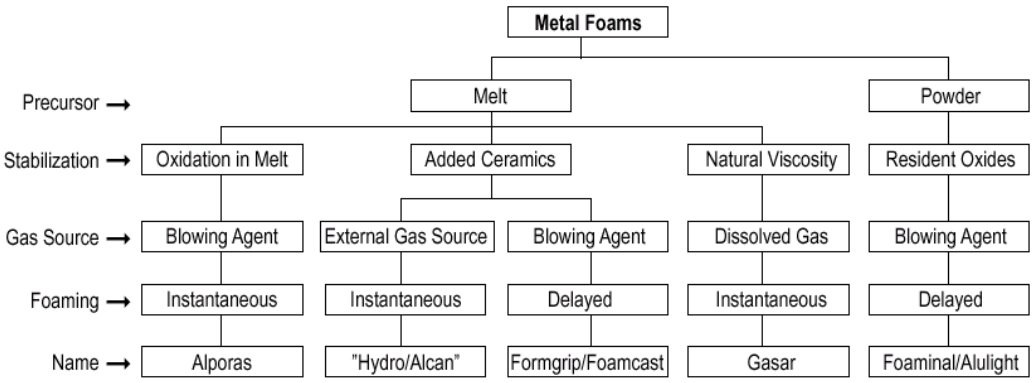

Figure 2.2: Classification of metal foam production techniques [20]

The two types of aluminium foam analysed in this study, Alporas and AL003860 are prepared by the direct foaming of the melt and investment casting, respectively. The Alporas production technique is based on *in-situ* gas formation by the thermal dissociation of the blowing agent [21]. The scheme of the production process is depicted in Figure 2.3.

The investment casting used for the production of AL003860, Duocel or M-Pore employs a plaster mould, which is removed after the cellular network is created (see Figure 2.4) [20].

Cellular solids are able to absorb significant amounts of deformation energy [22, 23] during impacts with the possibility to introduce strain-rate dependent characteristics into their deformation response, which contributes to the tunability of such materials. In 2001 Dannemann [12] studied the strain-rate dependent behaviour of the Alporas closed-cell aluminium foam and the Duocell open-cell aluminium foam Duocel. The investigated materials were subjected

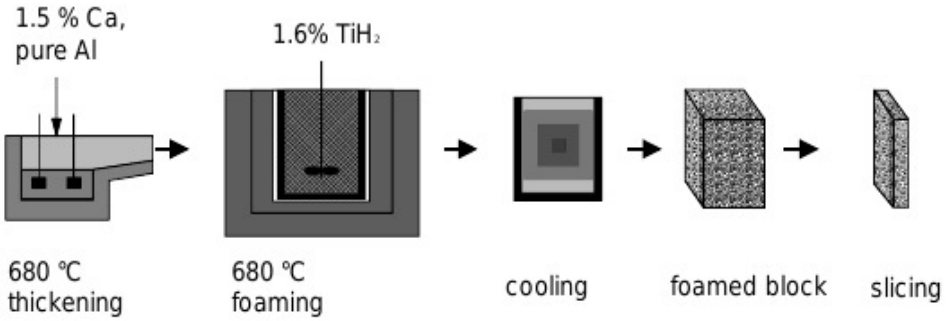

Figure 2.3: Production scheme of Alporas aluminium foam [21]

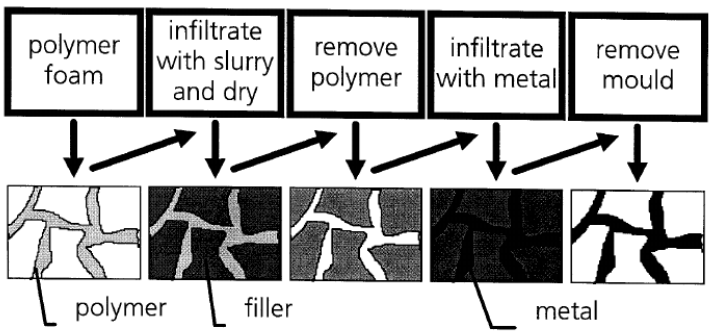

Figure 2.4: Investment casting process [20]

to compressive loading at strain-rates up to $2500\,s^{-1}$. Then, the stress-strain curves were compared as well as the nature of the cell damage mechanisms. Besides the description of the force-displacement or stress-strain dependencies, the mechanisms of the failure of the cellular structure was studied during the macroscopic investigation. Several studies reported a strain-rate sensitive mechanical response in the mechanical properties in polyurethane foams [24, 25, 26].

2.1.2 Meta-materials

Since cellular metals themselves are of limited compressive strength, they are disqualified for some energy absorption applications (e.g. blast protection) [27]. The decreasing stiffness and strength which occurs with the reduction in the relative density may be overcome in micro-architected materials, where a periodic lattice, the synergistic effect of the present phases allow one to keep

the specific stiffness and strength at desired level [28]. Such a class of materials are called meta-materials.

Recently, additive manufacturing enabled the preparation of a broader spectrum of meta-materials with a tailored geometry to achieve the desired mechanical properties [29]. Direct Metal Laser Sintering is an important group of additive manufacturing [30], which enables one to manufacture lattices with tailored geometry from different types of metal powder. This brought high stiffness, strength and ductility to the additively manufactured lattices. A group of hybrid foams, prepared from cellular solids (metallic or polymeric), surface of which is equipped with metallic coating is an example of mechanical meta-materials. In such materials, the favourable properties of the open-cell foam (controlled properties, simpler fabrication) are enhanced with the strain-rate dependency in the deformation behaviour, which is induced by the coating. The preparation and testing of the hybrid foams has been reported by Jung [31, 32, 33]. The technique of metallic coating may be also applied to additively manufactured lattices to further enhance of the mechanical properties.

Meta-materials are also represented by (but not limited to) inter-penetrating phase composites (IPC) or auxetics.

2.1.3 Inter-penetrating phase composites

Interpenetrating Phase Composites (IPCs) belong to a special subcategory of composite materials. In contrast to the well-established classes of composites, where a continuous phase (matrix) and a discrete phase (fibres or particles) is present, IPCs are composed of two continuous phases. The properties of the fibre reinforced composite strongly depend on the relation between loading direction and fibre orientation and decrease significantly in the transversal direction. In contrast, the continuous reinforcing phase in IPCs may exhibit mechanical properties without such anisotropy. Hence, IPCs offer enhanced properties compared to the more common particle or fibre- or particle-reinforced composite materials [34].

In IPCs, the energy absorption capabilities are enhanced by the synergistic effect of the cellular solid and filling material. In 2004, Gong [35] reported a study on a preparation of an IPC (or, more specifically, a metal-porous polymer composite, MPPC) and its testing under moderate strain-rates.

In 2006, Liu [36] considered Aluminium-polyethylene (Al-PE) and Aluminium-Epoxy (Al-Ep) composites manufactured using the infiltration method (vacuum assisted low negative pressure moulding process). Two important characteristics were revealed during the experimental compressive testing. The Al-Ep with 63% polymer exhibited a multifold increase in the plateau stress comparing to pure aluminium foam. The Al-PE specimen with the same volumetric content of polymer showed slightly higher plateau stress when compared to the pure foam but the plateau was extended up to a 75% strain before densification begun. Compared to the pure foam, both MPPC materials were also superior in terms of energy absorption capabilities.

Regarding the flexural characteristics of IPCs, Dukhan [37] tested aluminium-polypropylene foam samples with different pore densities and concentrated his work on the determination of the flexural stiffness and strength. A comparison with either of the base foam materials showed the superior properties of the MPPC and higher flexural stiffness with a decreasing pore size.

Periasamy [38] considered a syntactic-aluminium foam compressed at strain-rates of $0.001\,\mathrm{s}^{-1}$ and $1500\,\mathrm{s}^{-1}$. The IPC samples showed better compression characteristics and higher absorbed energy than the syntactic foam and the material exhibited strain-rate dependent energy absorption characteristics by adding an interpenetrating polymer phase to the open-cell aluminium foam. In recent studies, the strain-rate sensitivity and impact energy absorption capabilities of polymeric materials (both solid and cellular) were investigated. Luong [39] experimentally tested, at strain-rates up to $2000\,\mathrm{s}^{-1}$, the strain-rate sensitivity of PVC foams and observed increasing plateau stress value as well as a strain-rate sensitivity depending on the strain-rate with an increasing density in the PVC foam.

2.1.4 Auxetics

Auxetics are a class of meta-materials, which exhibit mechanical properties beyond the ranges of the base material due to geometrical properties of their lattice. Their lattice is constructed in such a way to exhibit a negative Poisson's ratio [40, 41]. For isotropic materials, Poisson's ratio may vary from -1 to 0.5, while, for anisotropic materials, the values of these limits do not apply [42]. This brings a wide range of tunable mechanical properties to such lattices. In the case of localised, penetrative, impacts, the structure is concentrated during

the deformation at the impact location and, thus, better resists the penetration. Due to this, the auxetic lattices have a high potential in impact protection, e.g. in a protective panel design. Among the manufacturing technologies of auxetics, additive manufacturing is of high importance as it enables one to prepare lattices with tailored properties [43].

Several studies were published, dealing with the response of the auxetics to mechanical loading under dynamic loading conditions. In 2002, Scarpa [44] published a comparative study of the crashworthiness of polymeric open-cell foams and auxetics under moderate velocity impacts and reported a substantial improvement in the auxetics' crashworthiness. In 2003, Scarpa [45] carried out a study on the mechanical response of polymer based auxetics focused on the visco-elastic behaviour. In another paper, the limited strength of polymeric auxetics at high strain-rate impacts was reported [46].

The performance of auxetics in impact energy absorption may be further enhanced by adding a strain-rate sensitive filling into the lattice. In such a case, a localised increase in the density together the properties of the filling material may increase the amount of the absorbed impact energy.

2.2 Multi-level characterisation of cellular materials

To assess the deformation response of cellular materials, standard macroscopic loading tests may be employed, which are well established for homogeneous materials as well. However, the well-established macroscopic test is not able to provide sufficient information on the mechanical response of cellular metals. To describe the mechanical behaviour in relation to the internal structure of the cellular materials, specialised experimental techniques are required, e.g. full-field strain measurement in a two- or three-dimensional manner or the mechanical testing of the basic elements of the cellular structures (i.e., cell walls or struts).

2.2.1 Properties of base material: micro-mechanical testing

For the characterisation of the base material of cellular solids, several techniques based on localised mechanical testing are available. One of the well established methods is indentation, which is able to measere penetration resistance in the materials' surface. Based on such results, the elastic and plastic properties may be derived. A special type of indentation technique, nanoindentation, uses instrumented indentation with a precise, sub-micrometre-sized indentation tip, with an applied load under 10 mN. Then, analytical laws, introduced by Oliver [47], may be used to derive Young's modulus and the other parameters of the material model. However, evaluation of the results of these techniques may be difficult as the methods are very localised. The fabrication techniques of cellular solids (both foaming techniques and additive manufacturing) induce local imperfections into the base material which may lead to the over- or underestimation of the base materials' properties assessed by the localised indentation techniques.

On the other hand, the testing of the individual cell-walls or struts, which are then considered as homogeneous, provides the effective properties of the base material. As the typical dimensions of the individual cells of the investigated materials are in the range of several millimeters or less and thickness of the cell walls reaches typically hundreds of micrometres, precise micro-scaled loading tests are required. The first reported efforts in the field of micro scaled tensile or bending tests started in the 1960s. However, the review of the history in the micro-scaled mechanical tests [48] reports the increase in successful experiments at this scale in late 1990s and at the beginning of this century connected with rapid improvements in the precise positioning and small-force measurements.

Micro-scale testing was succesfully applied to the experimental investigation of mechanical properties of individual *trabeculae*. This has been important for the trabecular bone research conducted by Jirousek [49] and Doktor [50] at the Institute of Theoretical and Applied Mechanics of the Czech Academy of Sciences. Testing devices designed for the purpose (in tensile and bending arrangement), were used for the research presented in the thesis for micro-scale tests of the base material of the cellular metal. The developed micro-scale loading devices are described in detail in Section 3.3 focused on a metal foam's

base material characterisation.

2.2.2 Optical strain measurement

Due to the complex geometry of cellular materials, the displacements and strains occurring under applied load are inhomogeneous. An optical observation of the deforming structure in conjunction with feature tracking allows one to overcome this issue. Moreover, the optical measurement provides a possibility to track the displacement in multiple points of the material's surface and map the strain fields. In 1981, Lucas [51] proposed a tracking algorithm based on the maximisation of the correlation coefficient between the pixel values in two subsequent images. This feature tracking method uses a search for the matching region in the image (subset) instead of the entire image, which improves the time demands of the algorithm. On the other hand, a sufficient size of the considered region is required to prevent a loss of correlation. A further improvement in the algorithm speed was brought using a weighting function. This prioritises searching for the tracking feature in the close vicinity of the original position of the feature. In 2010, Jandejsek [52] implemented the Lucas-Kanade tracking algorithm for Digital image correlation (DIC) in an in-house toolbox for the MATLAB computational environment, which enabled the further assembling of custom tools for data automated analyses of the obtained experimental data.

2.2.3 Time-lapse tomography

Another possibility on how to obtain detailed information about the deformation in the sample during a mechanical testing is to use X-ray computed tomography. The principles of X-ray computed tomography are based on X-ray imaging and Radon transform [53], which enables the reconstruction of the spatial image data from projections recorded at different angles. In 1982, Elliot [54] presented principles of X-ray computed microtomography with a high resolution (μCT). In this technique, the scanned sample rotates, while the source-detector pair remains stationary. To achieve the high resolution and enable the imaging of small samples, the μCT requires microfocus X-ray tube with a small spot and precise positioning stages. This enables one to reduce the angular increment during the scanning and to control the position of the imaging axes precisely. The principle of microtomography is depicted in Figure

2.5. Further enhancements of the reconstruction procedure were brought about by the introduction of a cone-beam reconstruction algorithm which takes into account the divergent nature of the X-ray beam into account [55].

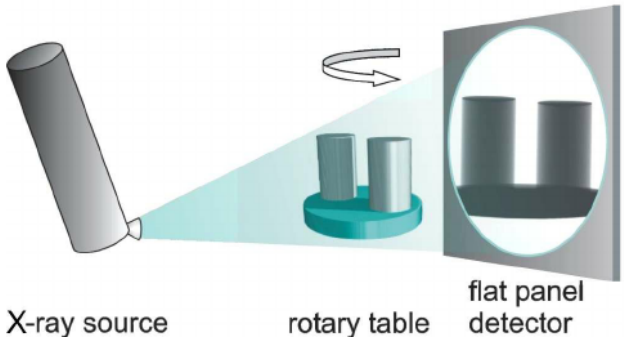

Figure 2.5: Principle of micro tomography (acquisition of the projections) [56]

In this dissertation, the tomographical measurements were performed in cooperation with the Instituite of Experimental and Applied Physics of the Czech Technical Univerity in Prague. This institute belongs to the leading workplaces in microtomographical measurements in terms of instrumentation for image acquisition as well as in implementation algorithms for the image data reconstruction. In 2006, Jakubek [57] designed and assembled a precise setup for microfocus X-ray tomography. In 2011, Vavřík [58] implemented a reconstruction algorithm which employs the theory of the cone-beam reconstruction in order to achieve an enhanced precision of the tomographic reconstruction.

In 2009, at the Institute of Theoretical and Applied mechanics, Zlámal [59] developed a software tool for the visualisation of tomographically scanned spatial image data which enables the direct conversion into the voxel models (note, that voxel is a three-dimensional analogy to the pixel).

In 2011, Jiroušek and Jandejsek [60] implemented the spatial extension of the Lucas-Kanade tracking algorithm for 3D strain mapping, digital volumetric correlation (DVC), proposed previously by Bay in 1999 [61]. In the DVC, the algorithm searches for the actual positions of the defined sub-volumes in consecutive sets of 3D image data. The defined sub-volumes in the reference (usually undeformed) sets of image data have to contain parts of the structure recognisable by the algorithm. Then, two steps of the tracking algorithm are performed. In the first step, integer values of the voxels' displacements are

found by the minimization of the normalised cross-correlation (NCC) coefficient using the steepest gradient method. In the second step, the deformation of each sub-volume is evaluated by the 3D extension of the Lucas-Kanade tracking algorithm [60]. The principle of DVC is schematically depicted in Figure 2.6.

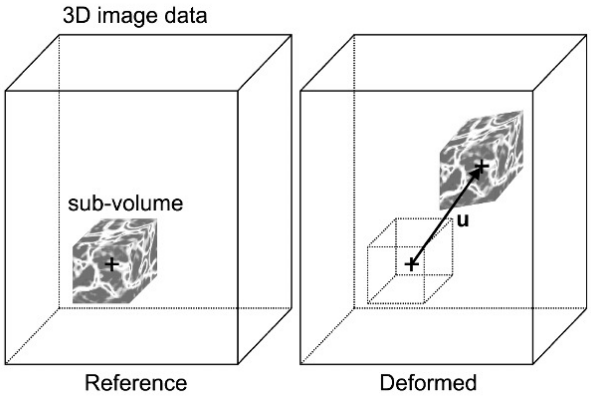

Figure 2.6: Principle of Digital Volumetric Correlation [60]

2.2.4 Inverse estimation of material model parameters using finite element analysis

For the description of material models of heterogeneous materials, the direct evaluation of the material parameter is usually not possible. However, numerical methods, e.g., Finite Element Analysis (FEA) can be used to estimate the parameters of the selected constitutive material model based on a comparison of a simple test and a prediction given by a simulation of the corresponding finite element model. With the increasing availability of the computational power in the late 1990s, coupling of the mechanical testing with the repetitively performed FE analysis of the corresponding mechanical tests was possible. This enabled the fitting of the constitutive model parameters for materials with complex microstructure or with a complex material models [62]. Different approaches in this field were developed over the last two decades, e.g., use of full-field displacement measurements and evaluation of such large sets of data by FEA [63] to obtain the material properties. Other studies focus on the methods for obtaining the best fit with reasonable computational complexity, e.g., use of a genetic algorithm or gradient techniques [64].

In this dissertation, the fitting procedure developed and implemented by Zlámal [65] is used to estimate parameters of a constitutive material model. The procedure is based on least squares method for minimising of the difference between results of experiments and FEA. During the fitting procedure, the FE simulation is performed repetitively with different values of material model constants and results of the simulation are compared with selected variables (e.g. displacement and loading force). Further details on the used fitting procedure are given in Section 3.3.4.

2.3 Dynamic testing

Since cellular metals should serve as energy absorbers, the description of the dynamic behaviour is required to utilise cellular metals in such applications. To obtain the dynamic mechanical properties testing at higher strain-rates is necessary. For testing at higher strain-rates, different, well established, methods might be employed. In this group of techniques, several were developed to provide single integral values, (i.e., the amount of the absorbed deformation energy) in each test (e.g., Izod test, Charpy test or drop-weight tear test) [66]. Universal testing machines with higher velocities, which use a servohydraulic control of the loading are nowadays available for loading rates and loading forces reaching dozens of metres per second and dozens of kilonewtons, respectively.

In this thesis, two methods were used for the dynamic testing at different strain-rates. For moderate strain-rate tests, drop tests were used. For high strain-rate testing, SHPB tests were used. Both the drop tower and SHPB were designed and assembled at our workplace with respect to the specific needs of the cellular materials' research.

2.3.1 Moderate strain-rate impacts testing

To assess the deformation response at a moderate strain-rate, drop tower may be employed, in which a dead weight is dropped onto a sample. A drop test is a well established setup, which provides the possibility to obtain materials' stress-strain curves, when the drop tower is instrumented with accelerometers and force transducer, or, preferably, in conjunction with an optical strain measurement. In the drop test, the impact velocity v and impact energy E_0 are controlled by the initial height h_0 and both the initial height and drop

weight m, respectively, according to Equations 2.1 and 2.2. Here, g denotes the gravitational acceleration. This poses a significant limitation for the achievable strain-rates.

$$v = \sqrt{2gh_0} \tag{2.1}$$

$$E_0 = mgh_0 \tag{2.2}$$

In [67], an example of the utilisation of a drop tower to measure the energy absorption capabilities of cellular metal is reported. At CTU FTS a drop tower was designed by Vyčichl in the framework of project SGS12/163/OHK2/2T/16 (originally designed for testing of bicycle and motorcycle helmets). Subsequently, this drop tower was customised by Fíla and Zlámal [68] for testing small scale specimens.

2.3.2 High strain-rate impact testing

To perform loading tests at strain-rates exceeding hundreds of s^{-1}, a Split Hopkinson pressure bar may be used. The technique which was developed by Bertram Hopkinson in 1914 [69]. This method that measures the mechanical response of a specimen at high strain-rates was based on the analysis of the strain wave propagating in a cylindrical bar. In 1949, Kolsky [70] improved this measurement technique by the arrangement of two bars in a series with a short specimen placed between the bars (see Figure 2.7). In the 1960's and 1970's, several additional arrangements were introduced, providing the possibility to perform testing in different loading modes (tensile [71], torsional [72]) aside the compressive mode, which the original design was intended for.

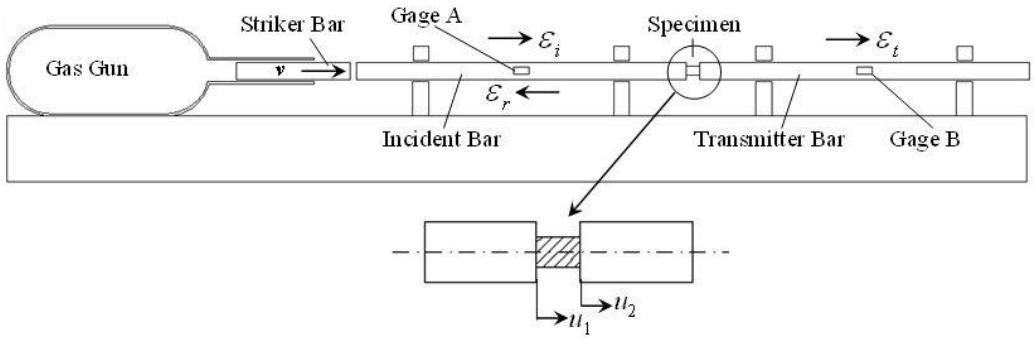

Figure 2.7: Scheme of Kolsky setup (SHPB) [73]

For the evaluation of the stresses and strains in the specimens tested using SHPB, an analysis based on the wave propagation theory is needed. In the experiment, a wave is generated in the incident bar by the accelerated striker. Then, the wave propagates in the incident bar until it reaches the incident bar-sample interface. Here, part of the strain wave propagates into the sample and transmission bar, while the other part is reflected into the incident bar.

The mathematical model to analyse the strain signals measured on the strain gauges, described, e.g., by Galina [74], yields Equations 2.3 to 2.5 to obtain the strain $\varepsilon_s(t)$, stress $\sigma_s(t)$ and strain-rate $\dot{\varepsilon}_s(t)$ in the sample based on the transmitted and reflected strain denoted by $\varepsilon_t(t)$ and $\varepsilon_r(t)$, respectively. Here, E is Young's modulus of the bars's material and c_0 is the wave propagation velocity of the bars. The geometrical characteristics (the length of the sample and the cross section areas of the sample and bars) are denoted by L_s, A_s and A, respectively.

$$\varepsilon_{\mathrm{s}}(t) = \frac{-2c_0}{L_s} \int_0^t \varepsilon_{\mathrm{r}}(t)dt \tag{2.3}$$

$$\sigma_{\mathrm{s}}(t) = E\frac{A}{A_{\mathrm{s}}}\varepsilon_{\mathrm{t}}(t) \tag{2.4}$$

$$\dot{\varepsilon}_{\mathrm{s}}(t) = \frac{-2c_0}{L_{\mathrm{s}}}\varepsilon_{\mathrm{r}}(t) \tag{2.5}$$

The original designs of the SHPB were equipped with metallic bars. Such bars exhibit elastic behaviour, hence, the wave propagation theory in elastic media was sufficient for the stress and strain calculations. On the other hand, metallic bars have high mechanical impedance, which poses serious issues for testing of low impedance materials (e.g. cellular materials or polymers).

To reduce the mismatch between the mechanical impedance of the bars and the tested specimen, use of viscoelastic bars was reported in the late 1990s by, e. g., Wang [75], Zhao [76] or Chen [77]. A comprehensive description on the mathematical background of the SHPB measurements using viscoelastic bars was introduced by Bacon in 1999 [78].

At our workplace, the design works on our SHPB apparatus begun in 2015 in the framework of the dissertation by Tomáš Fíla [79] and it was assembled in 2016. Subsequently, modifications and upgrades were made, e.g., a PMMA bars option, an OHPB option or arrangement for penetration tests.

2.4 Summary

In this chapter, an overview of the investigated cellular materials is presented, represented by closed- and open-cell cellular metals, together with examples of the enhancement of their impact response. The proposed applications of these materials include the impact energy absorption at different impact scenarios. A wide range of impact velocities (and corresponding strain-rates) is required to be covered by the tests. Aside the quasi-static tests, drop tests were selected to achieve strain-rates in range of dozens of s^{-1} and SHPB impact tests are used for strain rates up to range of 1000 to 4000 s^{-1}. Using these techniques cellular metals and additively manufactured auxetic lattices have been tested under impacts and effect of different fillers on the impact response have been evaluated.

Chapter 3

Structural properties and quasi-static mechanical response

In this part of the work, the quasi-static mechanical properties at a macroscopic and structural level were analysed. The aim of the experimental campaign was to obtain the loading response that a structural material has to pose in standard operating scenarios (i.e., a load bearing function). For a deeper insight into the structure and mechanical behaviour of the cellular material, a series of investigations focused on the detailed description of the structure and mechanical response of such a heterogeneous material is also included in this chapter. This includes the time-lapse tomography of uni-axial compressive tests and micro-scaled bending tests at the level of the individual cell-walls of the cellular metal. The description and results of these investigations were published in three author's papers: [80]* (time-lapse tomography of cellular structure compression) and [81, 82] † ‡ (micro-scaled mechanical tests of the base material of aluminium foam). Moreover, the quasi-static response was alsorequired as a reference for the assessment of the strain-rate dependent changes in the mechanical response of the tested materials. Therefore, for the conducted quasi-static tests, the sample shape, dimensions and preparation

*O. Jiroušek, **T. Doktor**, D. Kytýř, P. Zlámal, T. Fíla, P. Koudelka, I. Jandejsek, and D. Vavřík. X-ray and finite element analysis of deformation response of closed-cell metal foam subjected to compressive loading. *Journal of Instrumentation*, 8(2), 2013.

†**T. Doktor**, D. Kytýř, P. Zlamál, T. Fíla, P. Koudelka, and O. Jiroušek. Simulation of a three-point bending test on the isolated cell wall of aluminium foam. *Civil-Comp Proceedings*, 102, 2013.

‡**T. Doktor**, D. Kytýř, P. Koudelka, P. Zlámal, T. Fíla, and O. Jiroušek. Determination of elastic-plastic properties of Alporas foam at the cell-wall level using microscale cantilever bending tests. *Materiali in Tehnologije*, 49(2):203–206, 2015.

procedure corresponded to the respective samples' specification used by each dynamic testing scenario (drop tower tests, SHPB/OHPB tests). The descriptions of the specimen preparation, testing protocol as well as the results were published in the author's papers related to the dynamic testing [83, 84, 85].

3.1 Investigated materials

In the experimental studies, three groups of materials were tested: (i) cellular metals, (ii) polymeric filling materials and (iii) polymer-filled cellular metals - interpenetrating phase composites.

3.1.1 Cellular metals

Two types of cellular metal were used, the commercially available aluminium foams (i) Alporas (Shinko Wire, Corp., Japan) and (ii) AL003860 (Sigma Aldrich, Co. LLC, St. Louis, USA). The structural properties of both types of material declared in the producers' datasheets are listed in Table 3.1.

	Alporas	AL003860
Base Alloy	Al 99.5%, Ca 1.5%, Ti 1.5%	EN-AW-6101
Porosity [%]	91	93
Cell character	Closed	Open
Cell shape	Polyedric	Dodecahedral
Cell size [mm]	$4-6$	1.6
Cell wall/edge thickness [mm]	$0.07-0.1$	$0.35-0.50$

Table 3.1: Overall mechanical and structural properties of Alporas [8] and AL003860 [86]

3.1.2 Filling materials

Three types of filling materials were used in order to form the IPC together with the cellular metal or with the auxetic lattices. A polyurethane foam and polyurethane putty were used as a representative of the cellular and solid polymeric material, respectively. Moreover, ordnance (ballistic) gelatin was

used in the experimental campaigns. The ordnance gelatin is widely used as a soft tissue simulant for the assessment of the damage to tissues induced by bullets [87]. For this material, a strong strain-rate sensitivity under compressive loading was reported [9]. As the original ordnance gelatin is of organic nature, it poses a limited lifetime. However, there are also synthetic alternatives of the gelatin available, which exhibit a similar mechanical response, e.g., [88, 89, 90]. The detailed specifications and preparation procedures of the filling materials are presented in Section 3.4.

3.1.3 IPC

To assess the influence of the filling materials on the impact energy absorption capabilities, representatives of the IPC were tested under moderate and high strain-rates as well as under quasi-static conditions. Three combinations of IPC were tested: a cellular metal filled with a polyurethane putty and additively manufactured metallic auxetics filled with polyurethane foam and ordnance gelatin.

3.2 Time-lapse tomography of compression test

In order to observe the deformation response of the cellular material at the level of the microstructure, time-lapse tomography under mechanical loading was performed. A complex experiment with the Alporas foam specimen was performed. In the experimental study, the time-lapse μCT of a uniaxial compression test was used. The description of the experiment and its results were presented in the paper [80]. The tomographic measurements were performed in cooperiation with CTU IEAP.

3.2.1 Specimen preparation

The tested specimen was a prism with a 29×29 mm cross-section and a height of 56 mm. The dimensions were chosen according to the minimum size of a representative volume element (a cube with an edge length of 29 mm, described in detail by Koudelka [91]). The outer faces of the specimen were ground and polished to ensure the proper boundary conditions on the contact faces and to

avoid artifacts in the acquired image data. The specimen placed in the loading frame is depicted in Figure 3.1(a).

3.2.2 Loading procedure

A custom uniaxial loading device [92] was developed for the time-lapse tomographic measurements under an applied load. A material with low and homogeneous attenuation of X-rays was required for the part of the device where the sample is placed and irradiated. To comply with this requirement, a cylindrical frame was manufactured from a carbon fibre composite. The attenuation of the frame is lower than that of aluminium with a thickness of 0.03 mm. The loading is provided by a stepper motor with a harmonic drive and ball-screw actuator attached to the frame with a loading capacity of 25 kN. The device is depicted in Figure 3.1(b). The specimen was loaded incrementally in 4 steps up to a maximal force of 1.03 kN. A displacement controlled compressive test was performed. The first load step corresponded to an overall strain of 0.4% (this value was chosen in order to observe the material behaviour in its elastic regime) and three consequent steps corresponded to an overall strain of 1%, 2% and 3%.

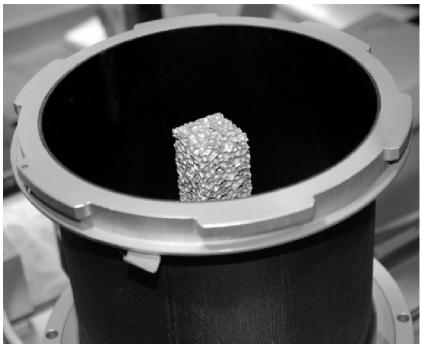

(a) Macrospcopic specimen (aluminium foam Alporas) inserted in the loading frame

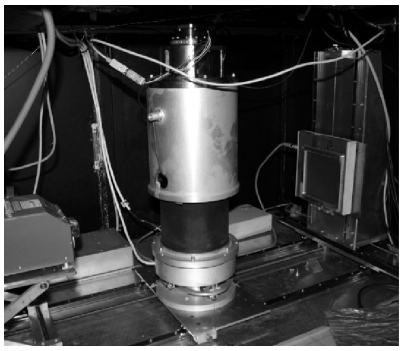

(b) Loading frame placed on a turntable in the X-ray shielded box (left: X-ray tube, right: flat panel detector)

Figure 3.1: Experimental setup for the time-lapse tomography of the compression test

3.2.3 X-ray imaging

Every deformation state (including the zero deformation state) was tomographically captured using a custom setup for X-ray microtomography [57] (see Figure 3.1b)). A Hamamatsu L8601-01 X-ray source (Hamamatsu Photonics K.K., Japan) and a Hamamatsu C7942CA-22 flat-panel detector was used. The physical dimensions of the detector are 120×120 mm and its resolution is 2240×2340 px. During the acquisition the target voltage was 70 kV and the target current was 140 μA. For the tomographic scanning of the initial state of the specimen 720 projections with an angular step of 0.5° and an acquisition time of 40×0.5 s were acquired. After every loading step, the tomography of the incrementally deformed sample using 360 projections (angular step 1°, acquisition time 20×0.5 s) was performed. To obtain the spatial image data from the acquired X-ray projections, a cone-beam reconstruction algorithm [58] was used. This reconstruction method accounts for the divergent character of the X-ray beam in both a horizontal and vertical plane. In the reconstructed volumetric data one voxel corresponds to a cube with an edge length of 21 μm. The reconstructed 3D microstructure of the Al foam is presented in Figure 3.2(a).

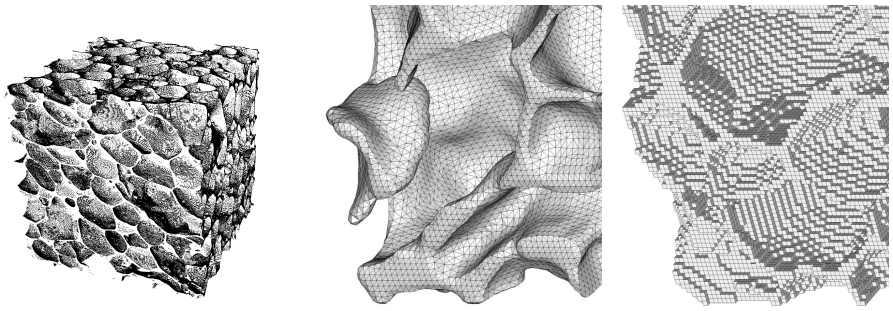

(a) 800 x 800 x 800 px (b) tetrahedral model (c) voxel model

Figure 3.2: Visualisation of the reconstructed CT image: central part of the sample (a), tetharedral mesh (b) and voxel model (c)

3.2.4 Digital volumetric correlation

To assess the displacements in the deforming cellular structure, the DVC technique described in [60] was employed. This method is based on a modified

Lucas-Kanade tracking algorithm [51] optimised for accuracy. A grid of points is defined in two sets of volumetric image data (reference and deformed). A subvolume around each point is used to calculate the updated position in the deformed image data. From the tracked displacements of the control points, it is possible to calculate the strain fields.

To define the set of points for the DVC, an FE model of the undeformed sample was developed using our in-house open source software tool **μCT vis&modeller** [59]. The model was composed of 81,976 tetrahedral elements with quadratic shape functions (required due to the low cell-wall thickness). The nodal points of the developed FE mesh were used as control points for the displacement tracking using DVC. This ensured the tracking of the points inside the cell-walls only, prevented the detection of zero displacements of points inside the voids and enabled a flawless comparison of the displacements obtained by the DVC and calculated by the FE simulation. Detailed part of the microstructure showing the difference between voxel and tetrahedral representation is shown in Figure 3.2(b) and (c).

3.2.5 Results

Four loading steps were investigated to obtain the complex information about the deformation of the sample. From the acquired data, an FE model with 81,976 tetrahedral elements was developed. To obtain the full displacement map of the deformed metal foam structure, a custom software for DVC was employed. To ensure the readability of obtained the results, a procedure to correct tracking points with lost correlation was suggested. If a point with a lost correlation was detected, the unknown displacement is replaced with the average displacement of its neighbours. The displacement fields for every loading state are depicted in Figure 3.3.

3.2.6 Concluding remarks

For a deeper insight into the deforming structure, a compression test together with a time-lapse X-ray tomography was used. Using a precise reconstruction procedure a detailed model with resolution 21 μm was obtained, which corresponded to $\frac{1}{4}$ of the cell-wall thickness. The DVC was applied to calculate the displacements in the deforming microstructure and to identify places with

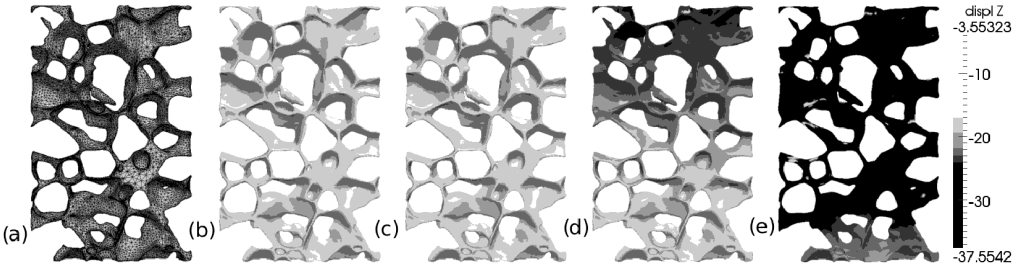

Figure 3.3: Results of the DVC on the image data acquired by the time-lapse tomography

high strain concentrations. Usually, DVC requires a random pattern in the volumetric image data, in this study, it has been proven that the complex microstructure of a cellular material (e.g., metal foam) is a sufficient basis for the algorithm.

3.3 Micro-scale loading tests

A series of micromechanical loading tests was performed in order to describe the mechanical properties of the base alloy of the metal foam. The tests were performed in a bending arrangement with two types of boundary conditions (i) three-point bending, (ii) cantilever bending. The tested specimens were extracted from the Alporas foam cell-walls. The results of these studies were presented in papers [81] and [82].

3.3.1 Specimen preparation

For the micromechanical tests, a set of specimens was extracted from the cellular structure. The sample extraction was performed in three subsequent steps. First, the vicinity of one cell was extracted from the structure (dimensions approximately $5 \times 5 \times 5$ mm). In the extracted region, a cell-wall with a minimal curvature was identified and extracted using a hand operated micro-lathe (FortiFlex, Dremel Europe). Finally, the isolated cell-wall was machined by a grinding machine to achieve a rectangular shape and to mechanically detach the zones mechanically influenced by cutting. Prior every distinct step of the preparation procedure, the specimen was embedded into rosin to prevent any plastic deformation of the specimen. Violin bow rosin was used for the purpose

due to its high purity and transparency and due to its low melting point (lower than 85 °C) minimising the risk of thermally influenced zones induced into the specimen.

Description of specimens' geometry

Due to the irregular specimens' shape, a detailed description of their volumes was required. In our previous studies dealing with the micromechanical testing of an isolated human trabeculae, a shape-form-silhouette reconstruction method was employed [93]. This technique is based on the inverse Radon transform performed on optical turntable projections of the specimen. However, the accuracy of this reconstruction decreases significantly for shapes with edges.

Shape representation. Since the cell-wall specimens exhibit two predominant dimensions (length and width) and a low thickness, the shape was simplified to a general quadrilateral representing the top view of the specimen and quadrilaterals representing 25 cross-sections of the specimen, uniformly distributed along the longitudinal axis. The vertices of the quadrilaterals were identified in three SEM projections for each sample.

Image data acquisition. After achieving the desired shape of the specimen, all the rosin used during the sample preparation was carefully removed by 96 % ethanol. The specimen was then scanned in a scanning electron microscope (SEM) MIRA LMU (Tescan, a.s., Czech Republic) using a secondary electron probe. For each specimen, the three projections mentioned hereinbefore were acquired.

Volumetric model reconstruction procedure. The volumetric model was obtained using a semi-automatic procedure developed in the MATLAB environment (Mathworks, Inc.). The curvature of the specimen was recorded based on the longitudinal projection by the manual picking of the silhouette in defined steps along the longitudinal axis. Several additional geometrical characteristics, e.g., support span, position of the loading tip and properties of the cross-section in the loading point were determined as well. The SEM projections and the loading scene are depicted in Figure 3.4.

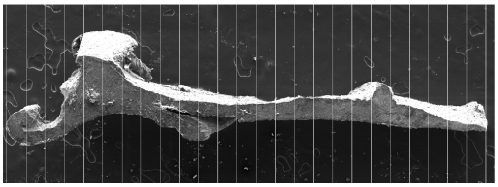

(a)

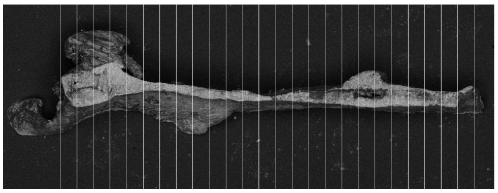

(b)

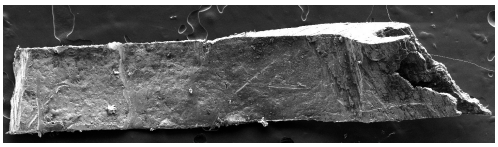

(c)

Figure 3.4: Single-wall specimens used in micromechanical experiments (three-point bending): longitudinal faces (a, b) and floor-plan projection (c) of the tested specimen acquired by SEM. Loading scene captured by CCD camera (d)

Boundary conditions

For the strain calculations in the micro-scale tests, as well as for the inverse FE simulations, it was necessary to properly define the exact positions of the supports and the loading tip for each individual sample. This was essential for the comparison with the experiments, due to the very small dimensions of the samples. It is important to realise, that even a very small deviation in the boundary conditions (BCs) or the loading tip position results in a significant change in results (stress, strain values).

To define the boundary conditions of the performed tests, i.e., position of the supports and the loading tip, a semiautomatic procedure was employed using projection of the loading scene. In the projection, the position of the supports and the loading tip were recorded relative to the ends of the specimen. Based on the obtained relative positions, the coordinates of the nodal points were derived in the model and the corresponding degrees of freedom of these nodes were removed.

3.3.2 Loading device

For the loading at the micro-scale level a custom modular loading device was designed and assembled. The conception of this modular loading device originated from a loading device with a tensile arrangement developed for testing of isolated trabeculae extracted from the human bone [49]. The first version of the device in a three-point bending arrangement [50] is depicted in Figure 3.5.

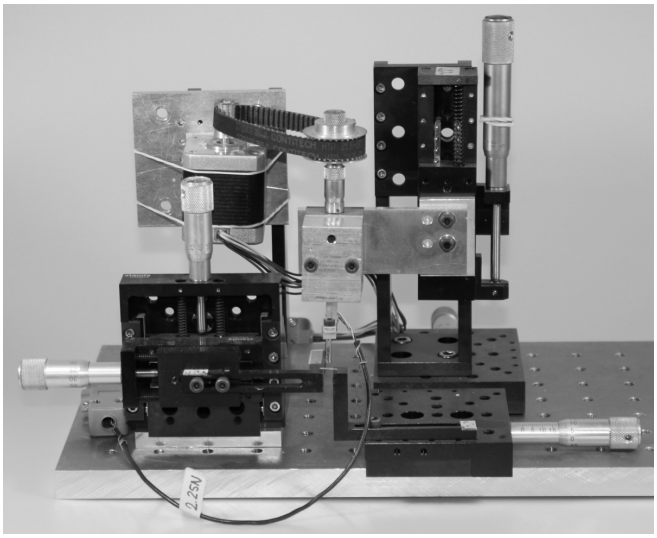

Figure 3.5: Original three-point bending experimental setup developed for testing of the human trabeculae

Since the tested trabeculae are of similar dimensions as the extracted cell-walls, only slight modifications were required to enable the presented tests. Due to the larger contact faces in comparison with the testing of the trabeculae, the friction between the supports and the sample became to be more significant and, in the preliminary tests the supports themselves exhibit significant bending which affected the measured deflections. Due to this fact a new design of the supports was suggested to achieve a significant increase in their stiffness as well as to ensure the proper radii for the rolling of the specimens' surfaces on the support to avoid longitudinal stresses in the specimen. The improved design of the supports is depicted in Figure 3.6.

Due to the significantly lower values of the reaction forces in comparison with the loading of the single trabeculae, the load cell was replaced with a new

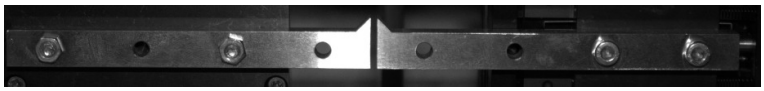

Figure 3.6: Improved design of the supports for the three-point bending tests

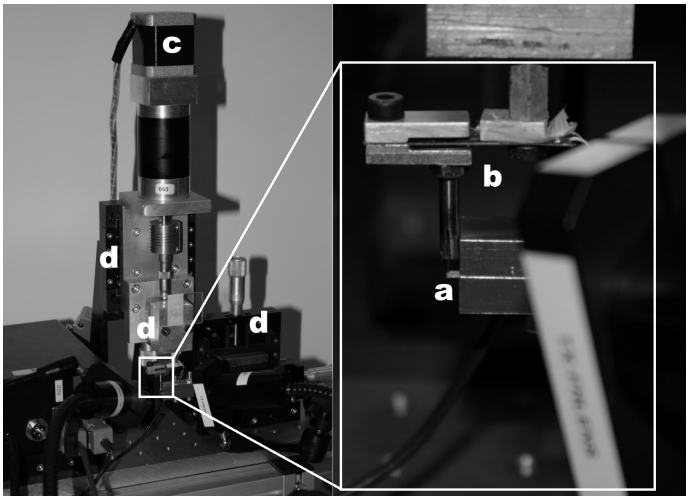

Figure 3.7: Loading setup for cantilever bending test. Sample (a), load cell (b), stepper motor attached to a flexible coupling (c), linear positioning stages (d)

one having a two times lower loading capacity (2.25 N) and providing two times higher sensitivity. The load cell was of the same arrangement, hence the replacement did not require further adjustments to the modular loading device. To enable a more precise displacement control of the tests, the belt drive was replaced by a harmonic drive. The ratio of the harmonic drive was 500:1 which corresponded to 400 steps per revolution. For the micro-scale tests in cantilever arrangement, another modification of the loading setup was used. This setup is depicted in Figure 3.7

3.3.3 Strain measurement

Due to the high compliance of the load cell (the deflection of the end of the load-cell was even higher than the displacement of the loaded point of the specimen), the strain was not able to be determined directly from the displacement prescribed be the linear bearing stage. The strains were measured optically using the tracking of the selected features in the projections of the loading scene.

Image acquisition setup

The set of projections of the loading scene was captured by a CCD camera (Manta G504B, Allied Vision Technologies, GmbH, Germany) with a resolution of 2452×2056 px. The camera was attached to an optical microscope (Navitar Imaging, Inc., USA) which provided magnification up to 24×. The acquisition of the projections was controlled by a custom software-tool developed by Zlámal [81] based on OpenCV [94] (Open Source Computer Vision) library [94]. The acquisition rate of the camera was 2 fps, which enabled, along the selected loading rate, a sufficient number of points on the force-displacement curve. Some examples of the loading scene are depicted in Figure 3.8.

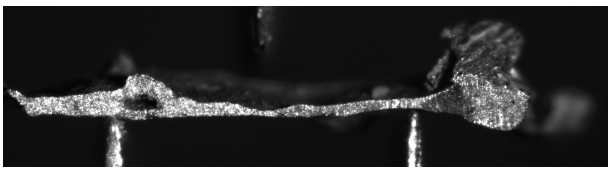

(a) Three-point-bending

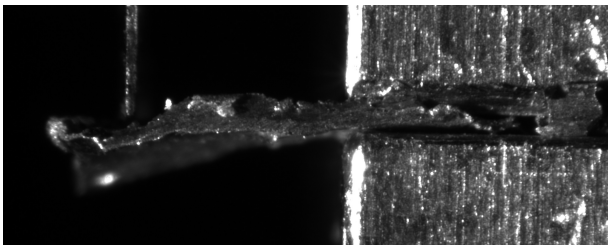

(b) Cantilever bending

Figure 3.8: Detailed image of the tested specimen placed in the loading device

Digital image correlation

From the sets of projections, the displacements were determined using the digital image correlation (DIC) software tool [52] based on the Lucas-Kanade tracking algorithm [51]. The position of the tracking features on the specimens' surfaces were selected in the vicinity of the loading point and the displacements were tracked by searching for the highest correlation coefficient between two consequent projections. The displacement paths of the tracked points in the selected test are depicted in Figure 3.9.

The evaluation procedure of the displacement paths is based on a set of shell scripts (assembled for the shell interpreter GNU Bash). It includes the

interactive selection of the region of interest in the measured force-displacement log, the selection of the tracking features, the launching of the digital image correlation procedure and the evaluation of the engineering strain and stress from the dimensions of the specimen and the geometrical arrangement of the loading test.

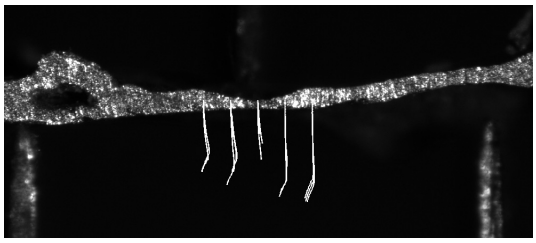

Figure 3.9: Displacement paths tracked by DIC

The engineering stress and strain values were determined from the geometrical properties of the tested specimen and optically measured displacements of the loading point using the formulae (3.1) and (3.2), which are based on the Bernoulli beam theory and the geometry of cantilever beam arrangement.

$$\varepsilon_{eng} = \frac{3uh}{2l^2} \tag{3.1}$$

$$\sigma_{eng} = \frac{Flh}{2I_Z} \tag{3.2}$$

Here, u denotes the displacement of the loading tip, h is the height of the specimen, F is the loading force, l is the distance between the clamp and the loading point and I_Z is the axial quadratic moment of inertia of the loaded cross-section. From the slope of the unloading phase, Young's modulus was determined and the yield point was estimated using the offset method at a 0.2 % strain level.

3.3.4 Inverse finite element analysis

Volumetric model development

The volumetric models used in the inverse FE simulations were obtained by the same procedure, which was used for the sample geometry description for the evaluation of the micro-scale bending tests. The procedure was presented earlier, in Section 3.3.1.

Simulation of three-point bending test

The volumetric model developed from the set of SEM projections was discretised (Figure 3.10) by the tetrahedral elements with the quadratic shape functions. This type of element was selected due to the highly irregular specimens' shape. An elasto-plastic material model with a von Misses yield criterion and bilinear isotropic hardening was used for the simulations. This model describes the deformation behaviour of the material in both the linear and post-yield phase of the loading. It is defined by four characteristics: Young's modulus and Poisson's number for the elastic part and yield stress and tangent modulus for the plastic region. The boundary conditions consistent with the experiment were prescribed in the simulation. The displacement controlled loading was simulated and, in the distinct loading steps, the reaction force in the loading point and the deflections of the nodes corresponding to the correlation markers were recorded. The selected displacement map is depicted in Figure 3.11.

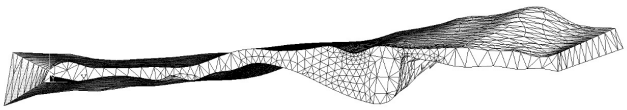

Figure 3.10: Example of the tetrahedral mesh of the isolated cell-wall tested in the three-point bending

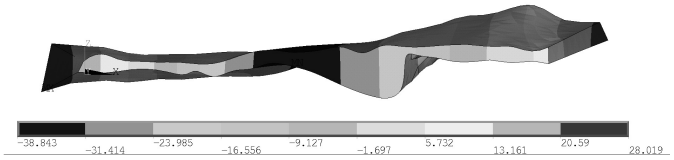

Figure 3.11: Example of the numerical results from the FE simulation of the three-point bending test: vertical displacements

Material model fitting

The elastic and plastic parameters of the model were varied to achieve a best fit with the force-displacement dependency measured in the bending test. The commercially available FEM software Ansys was used as the pre-processor, solver and post-processor. For the purposes of the inverse FE analysis, a set of software tools developed by Zlámal [65] were employed. This tool enabled

one to obtain an elastic-plastic material model based on the optimisation of the material constants in the repetitively performed simulation of the micromechanical test. The material properties are obtained in a two-step fitting procedure. In the first step, the initialisation loop, the constants of the material model are varied in expertly estimated ranges to achieve the minimum value of the least square error between the experimentally and numerically obtained displacements. In the second step (optimisation loop), three sets of material constants with the best fit (minimum of least square error) are selected. Based on the selected sets, the ranges for the optimisation are generated, using a Gaussian distribution with a mean in the values obtained in the initialisation loop [95].

3.3.5 Results

Three-point bending

Using a highly customised loading setup developed for the testing of the samples at the micro-scale level, the smooth force-displacement dependencies were observed (see Figure 3.12) with clearly a visible linear part followed by a yield point and plastic deformation. However, the values of Young's modulus vary significantly among the set of the measured samples (as listed in Table 3.2) and differ from the characteristics reported by several experimental studies (e.g., Němeček and Králík [96, 97]), where nanoindentation was employed. Some possible reasons of this discrepancy were considered in (i) the overestimation of the sample volume, (ii) presence of the influenced zone on the longitudinal edges caused by the specimen preparation or (iii) the improper simulation of the boundary conditions.

A further study was performed to quantify the influence of the preparation procedure on the mechanical properties of the base material of the metal foam [98] No significant influence was proven.

Cantilever bending

The stress-strain curves obtained by the cantilever bending test are presented in Figure 3.13. The curves exhibit similar slopes in their initial parts as well as in their unloading phases. The different portions of the plastic strain are caused by the non-uniformity in the specimens' dimensions due to the highly irregular

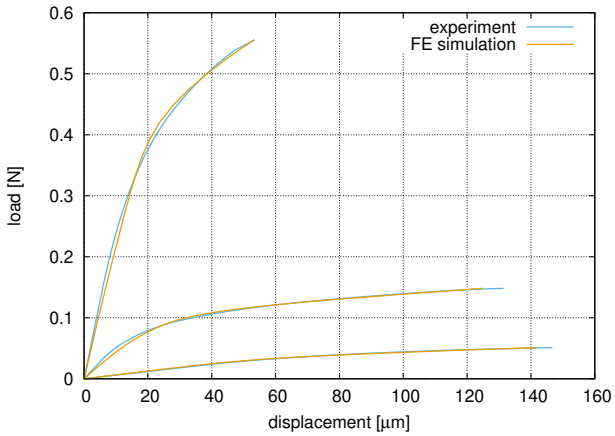

Figure 3.12: Results of the inverse FE simulation of the micro-scale three-point bending test

sample No.	Young's modulus [MPa]	yield stress [MPa]	tangent modulus [MPa]
1	29 015	52.538	2061.08
2	10 415	19.178	1376.58
3	54 399	88.408	1378.20

Table 3.2: Results of the inverse FE simulation of the micro-scale three-point bending test

geometrical arrangement of the cellular structure. The obtained values of the Young's modulus are 36.7 ± 5.2 GPa, the yield stress reached 39.0 ± 9.7 MPa and the yield strain reached 0.279 ± 0.044 %.

3.3.6 Concluding remarks

A series of micro-scale tests of a base material were performed in two different arrangements: (i) three-point bending and (ii) cantilever bending. The in-house experimental devices were successfully developed for this purpose and, for the precise strain measurement, the DIC technique was employed. The results of the three-point bending tests varied significantly among the set of specimens. On the other hand, the cantilever bending tests exhibited only a slight scatter in terms of the strength and stiffness of the tested material.

From the results, we can conclude that the cantilever bending tests are a more

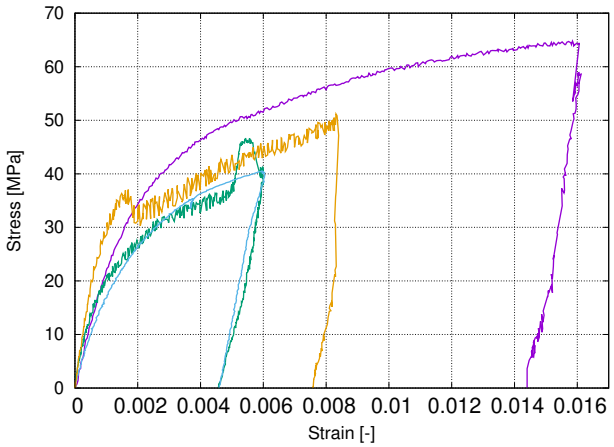

Figure 3.13: Experimental results of the cantilever bending tests

suitable technique than the simple supported beam test. This is contrary to the macrotesting, where the simple supported beam is preferred. The reason for this lies in the boundary conditions. For the cantilever test, the BC can be realised more accurately than in the case of the simple supported beam. The cantilever bending test is also not affected by the asymmetry of the loading tip, which affects the three-point bending tests.

3.4 Macroscopic quasi-static tests

In this section, the macroscopic quasi-static tests of (i) a cellular metal, (ii) an IPC and (iii) bulk filling materials are presented. As the results of these tests are later used as a reference for the further dynamic testing at different strain-rates (and, thus, using different experimental setups), the dimensions and preparation procedure varied among the sample groups. The experimental procedure as well as the results were, together with further dynamic tests, published in three papers: a comparative study of open cell aluminium foam and IPC at moderate strain-rates [83], testing of strain-rate sensitivity of ordnance gelatin at moderate strain-rates [84] and high strain-rate tests of different filling materials [85].

3.4.1 Specimen preparation

Cellular metal and IPC. For the comparative study between the cellular metal and IPC, two groups of samples were prepared. Prismatic samples with dimensions of $50 \times 30 \times 30$ mm were cut from the delivered slabs of the foam (their dimensions were limited by the size of the delivered slabs). One set of samples was kept in the "as delivered" state while the second group was filled with a one-component thixotropic polyurethane putty to form the IPC with a strain-rate sensitive mechanical behaviour. The comparison between the plain aluminium foam and the filled structure is depicted in Figure 3.14. In order to enable the optical strain evaluation using DIC, one face of each sample was polished and sprayed using granite paint to create a random pattern for the automatic displacement tracking.

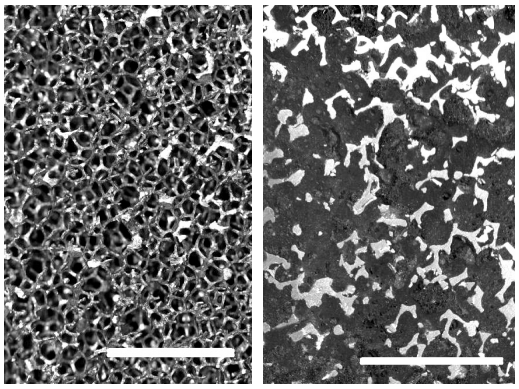

(a) "as delivered" foam (b) IPC

Figure 3.14: Specimen of the AL003860 open-cell foam. The scale bars correspond to 10 mm

Ordnance gelatin for impact tests. The ordnance gelatin for this campaign was prepared according to the reports of Jussila [99]. As a base, 260 Bloom beef gelatin (REMI MB, Ltd., Czech Republic) was used. The gelatin powder was poured into warm water (the temperature was 45 °C)

The samples were cured for 24 h at room temperature and subsequently stored for 24 h in a refrigerator. After this curing, the blocks were cut into samples of the desired size ($25 \times 25 \times 50$ mm). The dimensions of the samples

were limited by the diameter of the used loading plates. To ensure a better focus during the optical observation, the captured face of each sample was sprayed with granite paint to obtain a random pattern.

Bulk samples of filling materials. Three types of filling polymeric materials for the IPC were tested:(i) polyurethane foam, (ii) polyurethane putty and (iii) ordnance gelatin. Te cylindrical shape and dimensions (a diameter of 18 mm and a length of 5 mm) of the sample were selected with respect to bars' diameter in the SHPB apparatus. Both the polyurethane foam and polyurethane putty were commercially available single component substances which cured in several hours under ambient conditions. Due to its expansible nature, the polyurethane foam was poured into a larger mould and subsequently cut by a metallic hollow drill to the desired shape. Finally, the length of the cylinder was finalised by a sharp blade. The polyurethane putty was prepared in a confined mould, and after the curing process, the cylinders were shortened by a sharp blade.

3.4.2 Testing procedure

To obtain the reference stress-strain curves for the further evaluation of behaviour under higher strain-rates, a series of quasi-static tests of all three materials were performed. For the quasi-static tests, a custom uniaxial loading frame [100] with a loading capacity of 2 kN was used. The loading setup was instrumented by a load-cell U9b (Hottinger Baldwin Messtechnik, Germany) with a loading capacity of 1 kN. The loading was provided by a stepper motor attached to a harmonic drive and controlled by an in-house control software based on a LinuxCNC interface [101]. The loading setup for the quasi-static tests is depicted in Figure 3.15 together with its successor, which was used in the latter parts of this campaign [102]. A custom control unit for both the loading axis control and the load-cell readout was used [103].

The loading tests were displacement-driven and the final displacement corresponded to a strain up to 0.5, where the maximum travel range or loading capacity allowed for such a large strain value. Dependent on the sample height in each group, the loading rate varied from $4\,\mu\mathrm{m}\cdot\mathrm{s}^{-1}$ to $20\,\mu\mathrm{m}\cdot\mathrm{s}^{-1}$ to achieve a resulting strain-rate of $4\cdot10^{-4}\,\mathrm{s}^{-1}$. For the displacement tracking the loading scene was captured by a CCD camera (Manta G504B, Allied Vision

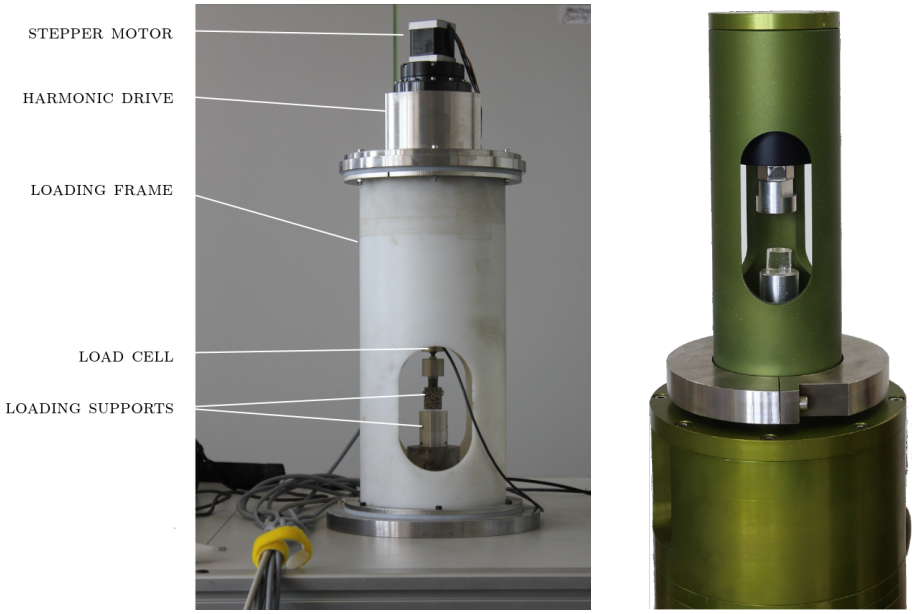

Figure 3.15: Experimental setup used for quasi-static tests.

Technologies, GmbH, Germany) attached to a bi-telecentric lens (TCZR 072, Opto Engineering, Italy). A custom read-out software based on the OpenCV library was used for the image acquisition. The resolution of the acquired image data was 2452×2056 px and the frame rate was 2 fps.

3.4.3 Results

From the quasi static loading test, the stress-strain curves were calculated based on the measured force F and displacements u tracked by DIC by the Equations 3.3 and 3.4, where A_0 is the specimen's cross-section and l_0 is the initial gauge length.

$$\varepsilon_{\text{eng}} = \frac{u}{l_0} \tag{3.3}$$

$$\sigma_{\text{eng}} = \frac{F}{A_0} \tag{3.4}$$

Then, the engineering strain ε_{eng} and stress σ_{eng} were then converted to logarithmic strain ε and true stress σ using Equations 3.5 and 3.6.

$$\varepsilon = ln\left(1 + \varepsilon_{\text{eng}}\right) \tag{3.5}$$

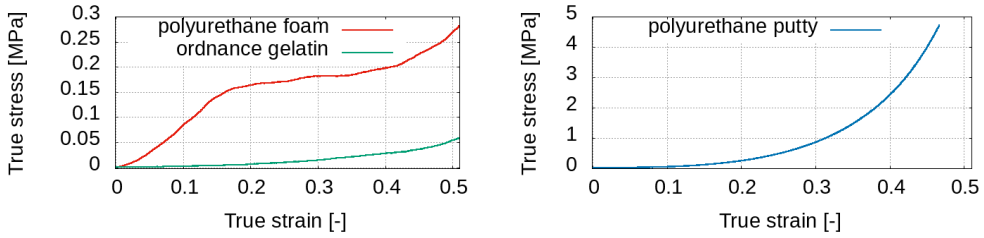

(a) Polyurethane foam and ordnance gelatin

(b) Polyurethane putty

Figure 3.16: Stress-strain curves of the representatives of filling materials.

$$\sigma = \sigma_{\text{eng}}(1 + \varepsilon_{\text{eng}}) \tag{3.6}$$

In Figure 3.16, the obtained stress-strain curves are depicted. In the mechanical response of the polyurethane putty, progressive densification occurred during the entire compression loading up to a strain of 0.45 . In the response of the polyurethane foam, the elastic region was observed up to a strain of 0.15 followed by a plateau up to a strain of 0.40 and the densification. The response of the bulk ordnance gelatin exhibits steady densification followed by a plateau region at a strain of approximately 0.25 .

The results of the quasi-static compression tests of the open-cell aluminium foam and IPC are presented in Section 4.2 (in Figures 4.4a and 4.5a). The cellular metal exhibited a short elastic region followed by an extensive plateau. On the other hand, in the case of the IPC, after a similar elastic region, the stress continued to increase with a lower tangent up to a strain of 0.12 .

3.4.4 Concluding remarks

A series of quasi static tests with the samples of the cellular metals and filling materials selected for the further dynamic tests were successfully carried out and evaluated. The obtained loading response corresponds with the theoretical assumptions described in the literature as well as with results reported in previously published studies. The characteristics related to the impact energy absorption (plateau stress, peak stress, strain energy density) were subsequently used as reference values in further experimental campaigns focused on the response at higher strain-rates.

3.5 Summary

The multi-level testing of the cellular materials presented in this chapter provides an insight into the mechanical response of cellular materials to loading. The mechanical tests at micro- and macro-scale level were carried out using custom developed loading devices and an optical strain measurement system. With these techniques, the sufficient precision of both stress and strain measurements was achieved. Coupled with the FE analyses, the multi-level mechanical testing helps to describe the relationship between the structural properties and the deformation behaviour. However, due to the heterogeneity of the cellular structure, the generalisation of such descriptions is challenging. In this work, the multi level mechanical test were limited to the quasi-static loading rates. Currently, our laboratory is being modernised to include the possibility of studying the internal structure of materials using a flash X ray technique, which will enable possibility of high strain-rate tests coupled with imaging of the inner structure during the impacts.

Chapter 4

Moderate strain-rate impact testing

As it was pointed out previously in the text, for the considered energy absorption applications, it is important to investigate the behaviour of a considered material under a broad range of strain-rates. For moderate strain-rates, slightly exceeding $100\,\mathrm{s}^{-1}$, drop tests are usually performed.

For this experimental campaign, an in-house drop tower was used. This drop tester was designed and assembled in the Department of Mechanics and Materials. The available impact velocities reach $5.85\,\mathrm{ms}^{-1}$ and the maximum available impact energy is 111.7 J. In this part of the work, the mechanical response and energy absorption properties of the open-cell aluminium foam as well as the ordnance gelatin and one representative of IPCs were assessed. The description of these experiments and their results were previously published in two author's papers [83] * and [84]†.

4.1 Experimental methods: Drop test

4.1.1 Impact test procedure

The impact tests were carried out in three arrangements with a different initial height and mass of the impactor. In each arrangement, a pair of samples

*T. Doktor, P. Zlámal, T. Fíla, P. Koudelka, D. Kytýř, and O. Jiroušek. Properties of polymer-filled aluminium foams under moderate strain-rate loading conditions. *Materiali in Tehnologije*, 49(4):597–600, 2015.

†T. Doktor, P. Zlámal, J. Šleichrt, T. Fíla, and D. Kytýř. Impact Testing of Ordnance Gelatin under Moderate Strain Rate Conditions. In 16TH *YOUTH SYMPOSIUM ON EXPERIMENTAL SOLID MECHANICS, volume 18 of Acta Polytechnica CTU Proceedings*, pages 44–47, 2018.

was tested. The initial heights and impactor masses are listed in Table 4.1 with the corresponding impact energy, velocity and strain-rate. The impact velocity was calculated using the initial height and gravity constant based on the conservation of sum of the kinetic and potential energy.

group	initial height $[m]$	drop weight $[kg]$	impact velocity $[m \cdot s^{-1}]$	strain-rate $[s^{-1}]$	impact energy $[J]$
1	1.00	4.495	4.43	88.6	44.1
2	1.50	4.495	5.42	108.5	66.1
3	1.50	6.504	5.42	108.5	95.7

Table 4.1: Impact test parameters - testing of the ordnance gelatin.

4.1.2 Instrumentation

The low energy compressive impact tests were performed by our laboratory drop tower (see Figure 4.1). The acceleration was measured by the tri-axial accelerometer (EGCS3, Measurement Specialties, USA) connected to the read-out electronics (9234, National Instruments Corporation, USA) with a sampling rate of $51.2\,\mathrm{kS \cdot s^{-1}}$. The strain was measured optically using a high speed CMOS camera (NX3, Integrated Design Tools, Inc., USA). The frame rate was 4770 fps and the resolution of the acquired images was 536×896 px. The exposure time for the "as delivered" group and for the IPC specimens was $49\,\mu$s and $19\,\mu$s, respectively. The longer exposure time was required due to a higher diaphragm number, which enabled one to extend the depth of field for the open cellular structure. Based on the results of the quasi-static compression, the amount of the absorbed energy was estimated in order to set an appropriate impact velocity for the low energy impact tests. For both "as delivered" and IPC specimens, the impact tests at three initial height levels were used: (i) 600 mm and (ii) 1000 mm. Additionally the initial heights (iii) 1400 mm and (iv) 1750 mm were used for the impact test of the filled specimen. The corresponding strain-rates are listed in Table 4.2 compared to the strain-rate prescribed in the quasi-static tests. The drop weight was 6504 g.

	initial height $[m]$	drop weight $[kg]$	impact velocity $[m \cdot s^{-1}]$	strain-rate $[s^{-1}]$	impact energy $[J]$
1	0.60	6.504	3.43	68.6	38.3
2	1.00	6.504	4.43	88.6	63.8
3	1.40	6.504	5.24	104.8	89.3
4	1.75	6.504	5.85	117.2	111.7

Table 4.2: Impact test parameters - testing of the cellular metal and IPC

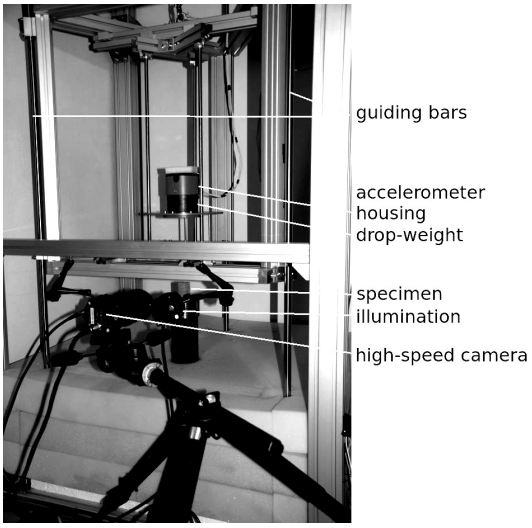

Figure 4.1: Drop tower developed at CTU FTS

4.1.3 Stress and strain measurements

Stress values $\sigma(t)$ were obtained from the measured acceleration $a(t)$, the mass of the impacting dead weight m and the cross-section of the samples A using Equation 4.1.

$$\sigma(t) = \frac{m \cdot a(t)}{A} \tag{4.1}$$

For both the quasi-static compression and low energy impact tests, an optical strain measurement was used. In the first image of each captured sequence, the tracking features were selected arranged in two horizontal lines in the lower and upper part of the specimen. Using a custom digital image correlation software [52] based on the Lucas-Kanade tracking algorithm [51] displacement

No. / group	strain energy density [Jcm^{-3}]	peak acceleration
1 / A1	1.04503	234.92g
2 / A1	1.00956	209.23g
3 / A2	1.12309	210.53g
4 / A2	0.98409	231.10g
5 / A3	1.42620	199.30g
6 / A3	1.69909	223.24g

Table 4.3: Impact test results - bulk ordnance gelatin.

paths were tracked. During the tracking procedure, the neighbourhoods of each tracking feature is searched for the highest correlation coefficient in the subsequent image. From the tracked displacements, the logarithmic strain was computed.

4.2 Results

Ordnance gelatin

The comparison of the stress-strain curves is depicted in Figure 4.2. For the assessment of the dissipated impact energy, strain energy density λ was computed from the strain ε and stress σ values using Equation 4.2. Note, that ε_{max} is the lowest value of maximum achieved strains among each evaluated set of samples.

$$\lambda = \int_0^{\varepsilon_{\max}} \sigma \, \mathrm{d}\varepsilon \tag{4.2}$$

The obtained strain energy density values are presented in Table 4.3. Moreover, for a visual evaluation of the deformation behaviour, the captured loading scene was used (the selected series of loading scenes in the distinct loading steps is depicted in Figure 4.3).

Cellular metal

From both the quasi-static and moderate strain-rate compression tests, the stress-strain diagrams were obtained. The stress-strain curves for the open

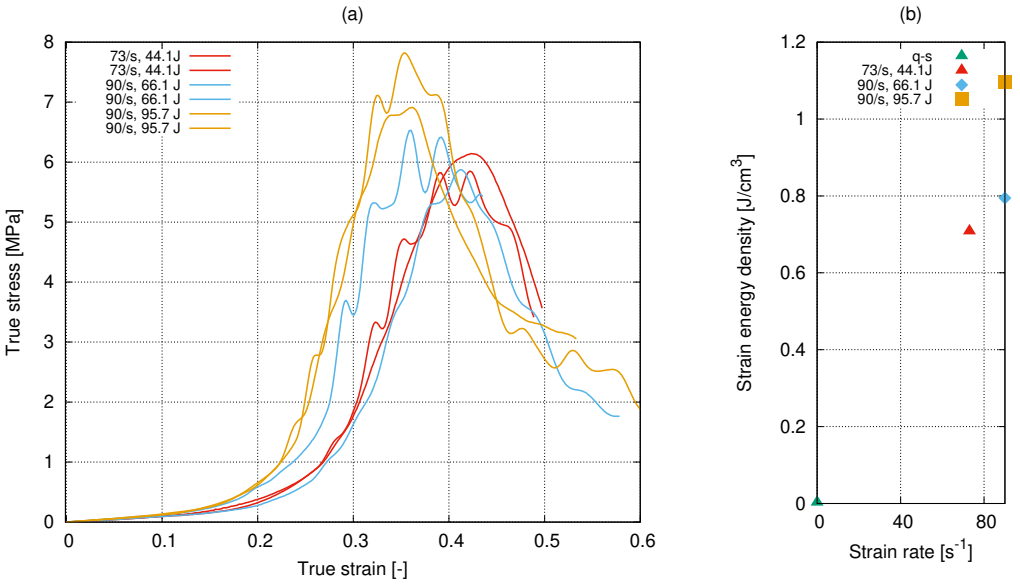

Figure 4.2: Results of the moderate strain-rate impact tests of the ordnance gelatin.

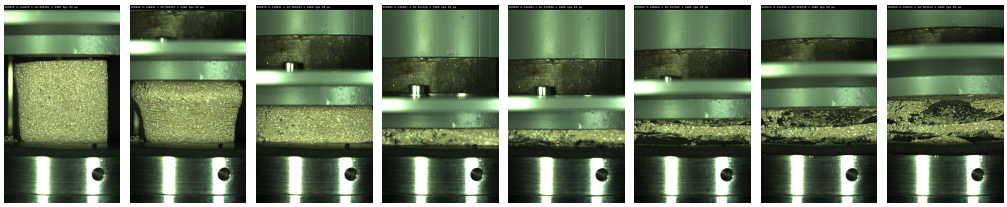

Figure 4.3: Loading scene of the selected sample (group A3) in several loading steps (the time step between the captured images is 0.89ms).

cell aluminium foam AL003860 are depicted in Figure 4.4. The stress-strain curves of the "as delivered" foam exhibit deformation behaviour of a typical cellular metal. The initial linear elastic part is followed by a constant stress plateau region caused by the collapse of the cell-edges during compression. Since the cell-edges in the entire microstructure collapse gradually, the plateau stress exhibits an insignificant scatter. As expected, the plateau stress is similar in both the quasi-static and dynamic loading. This is only valid only for the empty cellular structures. For the tested IPCs, the plateau stress is substantially elevated for higher strain-rates (see the following paragraphs).

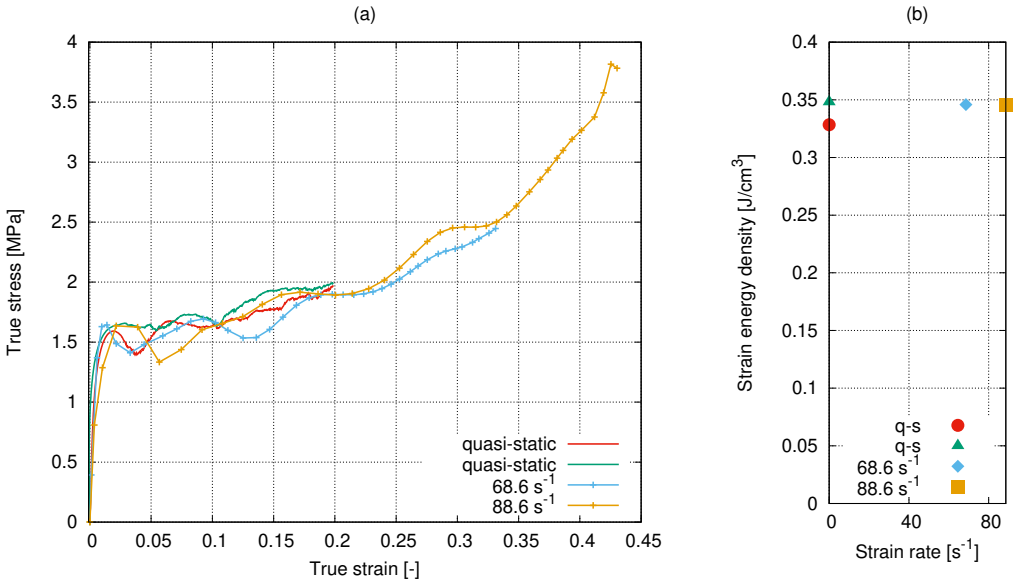

Figure 4.4: Results of the moderate strain-rate impact tests of the open cell aluminium foam.

IPC

The stress-strain curves for the impact test of the IPC (AL003860 filled with polyurethane putty) are depicted in Figure 4.5 (IPC). The deformation curves of the IPC samples showed a linear behaviour up to a stress level similar to the plateau stress of the plain foam followed by the apparent deformation of the polymeric filling represented by gradual increase in the stress in the compaction region. The amount of deformation energy absorbed during loading by the IPC samples increased in the non-zero strain-rate tests showing that such a material exhibits strain-rate dependent mechanical characteristics.
From the stress-strain curves of the compression tests, the deformation energy absorbed in the sample was determined. To enable a comparison among all the groups of specimens and levels of the strain-rates, deformation curves up to 21% were considered. The comparison is presented in Table 4.4.

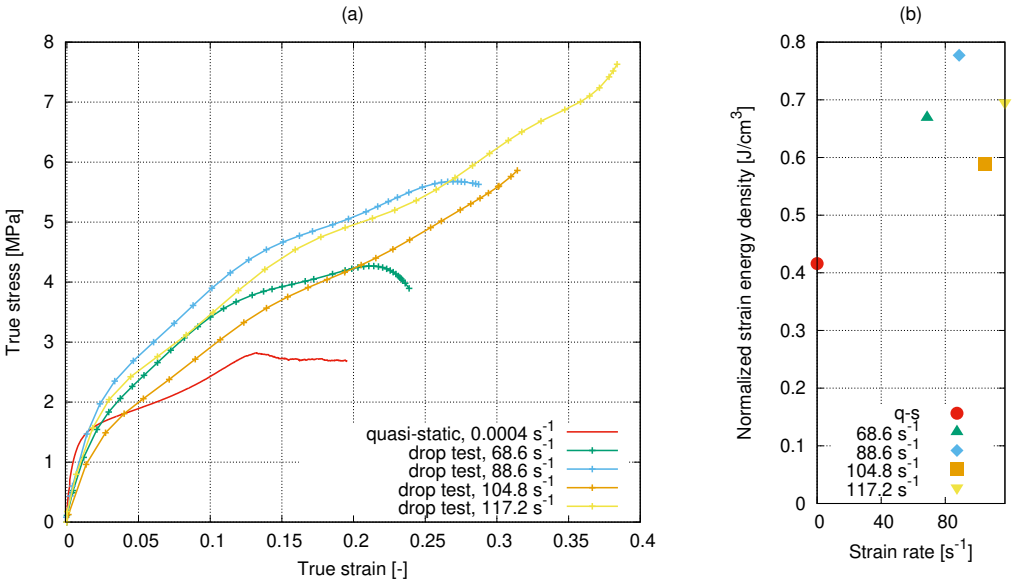

Figure 4.5: Results of the moderate strain-rate impact tests of the IPC.

material	test arrangement	strain energy density [J cm^{-3}]
Open-cell foam	quasi-static test	0.339 ± 0.014
Open-cell foam	drop test	0.327 ± 0.043
IPC	quasi-static test	0.452 ± 0.051
IPC	drop test	0.711 ± 0.078

Table 4.4: Comparison of the strain energy density up to 21% deformation

4.3 Concluding remarks

Ordnance gelatin

In the results of the impact testing of the ordnance gelatin, a significant strain-rate effect was observed in terms of the ultimate compressive strength and strain energy density. In comparison of the deformation behaviour under quasi static conditions and the drop weight test the difference was very significant. Moreover, a slight increase in both the strength and strain energy density was observed even between the different impact energies and velocities during the impact testing.

Cellular metal

The open-cell aluminium foam did not exhibit strain-rate sensitivity in the "as delivered" state in the range up to a strain-rate of 88.6 s^{-1}. The level of plateau stress did not change with an increasing strain-rate. The differences observed in the absorbed amount of impact energy are based on the increasing portions of strain induced by the higher levels of the impact energy.

IPC

On the other hand, the IPC based on the open-cell aluminium foam and polyurethane putty, showed a substantial increase in the absorbed impact energy at higher strain-rates in this case. While under the quasi-static loading, the IPC exhibits a plateau, at higher strains, a steady increase (with a lower slope) is observable in the stress-strain curves. The direct comparison of the specific absorbed energy (related to the density) between the open-cell metal foam and the IPC would not yield in a substantial increase of such a measure. However, in protective applications, where mass is not a critical parameter, the conjunction of a large strain energy density of the filler and plateau region of the foam (which limits the overall stress and lowers the slope of the resulting stress-strain curve) may be favourable.

Chapter 5

High strain-rate impact testing

For the assessment of the materials and their applicability in protective applications, where high impact velocities occur, a high strain-strain testing is required. For the description of the response at high strain-rates (up to thousands of s^{-1}), SHPB impact testing is one of the commonly used techniques.

In this chapter, the high strain-rate compressive tests of three representatives of the filling materials for IPC are presented. The description of the experimental procedure and the results presented in this chapter were published in the author's paper* [85].

5.1 Specimen preparation

For the testing of the filling materials, cylindrical samples were used with a diameter of 18 mm and a length of 5 mm. The dimensions were selected with respect to the dimensions of the SHPB apparatus. The procedure of the specimens' preparation was the same as for the quasi-static reference tests and is described in Section 3.4.1.
From the IPC (composed of the open-cell metal foam and polyurethane putty as described in Section 3.1.3), cubic samples were prepared with an edge length of 13 mm yielding in the diagonal length slightly shorter than the bars' diameter.

*__T. Doktor__, T. Fíla, P. Zlámal, D. Kytýř, and O. Jiroušek. High strain- rate compressive testing of filling materials for inter-penetrating phase composites. In *17th Youth Symposium on Experimental Solid Mechanics, YSESM 2018, volume 25 of Acta Polytechnica CTU Proceedings*, pages 21–24, 2019.

5.2 SHPB tests

For the high strain-rate tests, an in-house SHPB, developed at CTU in Prague [104] was used. The apparatus is based on the Kolsky setup, which was adapted for testing materials with a low mechanical impedance. To prevent a mismatch in the mechanical impedance of the bars and tested material, the striker, incident and and transmission bars were manufactured from a Poly Methyl-metacrylate (PMMA). The diameter of the bars was 20 mm, the lengths of striker, incident and transmission bars were 190 mm, 1600 mm and 1600 mm, respectively. The bars were supported by 8 low-friction polymer-liner slide bearings with an aluminum housing (DrylinFJUM housing, IGUS, Germany). The striker bar was accelerated by an air gun with a maximum pressure 16 bar with a fast release solenoid valve (366531, Parker, USA).

Different levels of barrel pressure were used to accelerate the striker in a range from 0.5 bar to 3.0 bar. The selected pressure levels were based on the preliminary tests and their results to induce a sufficient portion level of deformation in the tested groups of samples, respective to the tested type of material. The pressure levels of 0.5 bar, 1.0 bar and 1.5 bar were selected for testing the polyurethane foam and polyurethane putty, which resulted in striker impact velocities of $7\,\mathrm{m}\cdot\mathrm{s}^{-1}$, $11\,\mathrm{m}\cdot\mathrm{s}^{-1}$ and $13\,\mathrm{m}\cdot\mathrm{s}^{-1}$, respectively. The pressure levels of 1.0 bar, 2.0 bar and 3.0 bar were used for the samples of ordnance gelatin, yielding impact velocities of $13\,\mathrm{m}\cdot\mathrm{s}^{-1}$, $15\,\mathrm{m}\cdot\mathrm{s}^{-1}$ and $19\,\mathrm{m}\cdot\mathrm{s}^{-1}$, respectively. For the impact testing of the IPC, pressure levels of 3.0 bar and 7.0 bar were used, which accelerated the striker bar to velocities of $19\,\mathrm{m}\cdot\mathrm{s}^{-1}$ and $27\,\mathrm{m}\cdot\mathrm{s}^{-1}$, respectively.

The incident bar was instrumented with 3 measurement points using strain-gauges to take the wave propagation phenomena in visco-elastic medium into account. The transmission bar was instrumented with single measurement point. Foil strain-gauges (3/120 LY61, Hottinger Baldwin Messtechnik, Germany) were applied on each measurement point using a single component low-viscosity cyanoacrylate adhesive (Cyberbond 2003,Cyberbond Europe GmbH, Germany). The strain-gauges were connected in a Wheastone half-bridge arrangement to compensate for the possible minor bending of the bars during the latter stage of the experiment. The signals were amplified by an active differential low-noise amplifier (EL-LNA-2, Elsys AG, Switzerland) and recorded by a high speed 16-

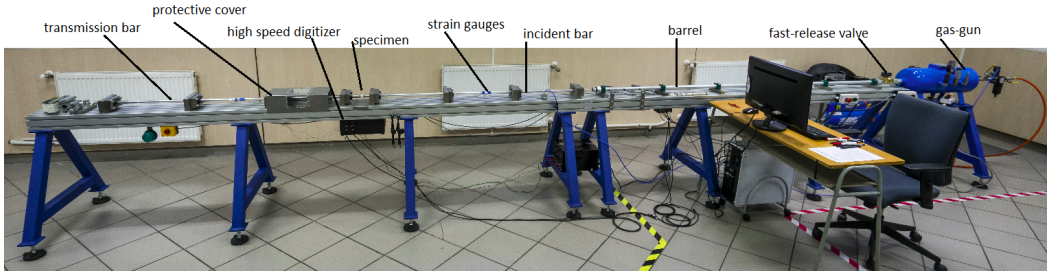

Figure 5.1: SHPB setup.

bit digitiser (PCI-9826H, ADLINK Technology, Inc., Taiwan) with a maximum sample rate of 20 MHz. Due to the limited capacity of the digitizer, the precise triggering of the measurement was required. The trigger was implemented by a pair of laser through-beam photoelectric sensor (FS/FE10-RL-PS-E4, Sensopart, Germany) which were installed on the barrel.

The acquisition of the strain-gauge signals was performed by the LabXHPB in-house software tool developed in the LabView environment [105]. Subsequently, the signals were analysed using the SHPB/OHPB evaluation tool created by Fíla [106].

A high speed camera (FASTCAM SA5, Photron, Japan) was used to capture the loading scene at a frame rate of 124 000 fps which enabled the visual inspection of the deformation behaviour of the tested specimens. The SHPB setup is shown in Figure 5.1.

5.3 Results

In the high strain-rate tests, the stress-strain curves were derived using the strain-gauge signals. In total, 5 tests were performed for every pressure level in each sample group. To check the validity of the performed tests, the force equilibrium (convergence between input and output force at transmission bar) was evaluated. An example of the equilibrium evaluation is presented in Figure 5.2.

The stress-strain diagrams for the group of the polyurethane putty, the polyurethane foam and the ordnance gelatin are presented in Figures 5.3a-5.6a. Note, that the strain-rate against strain is plotted for each level of impact velocity in the same figures. The strain-rate of the experiments varied from 1000 s^{-1} to 4000 s^{-1} for the different levels of the impact velocities and a nearly

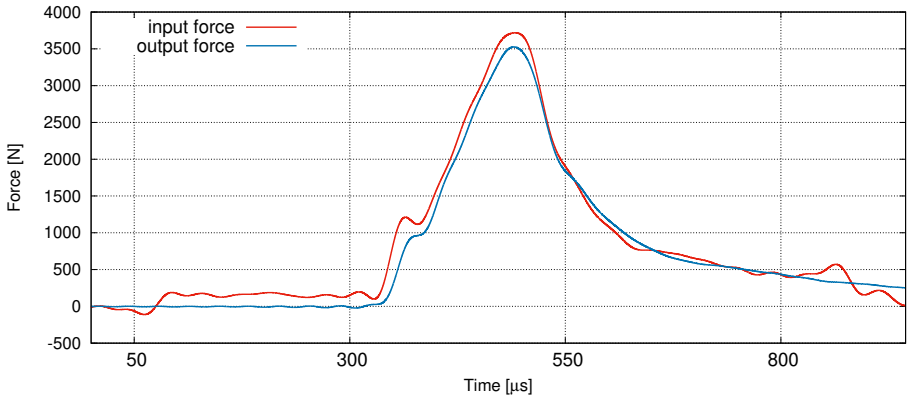

Figure 5.2: Example of the force equilibrium diagram for the polyurethane putty specimen tested at 1.5 bar.

constant strain-rate was achieved for all groups of samples during the deformation.

From the measured stress strain curves, the strain energy density was evaluated according to Equation 4.2. The obtained values of the strain energy density for each group and each level of the impact velocity are presented in the diagrams in Figures 5.3b-5.6b.

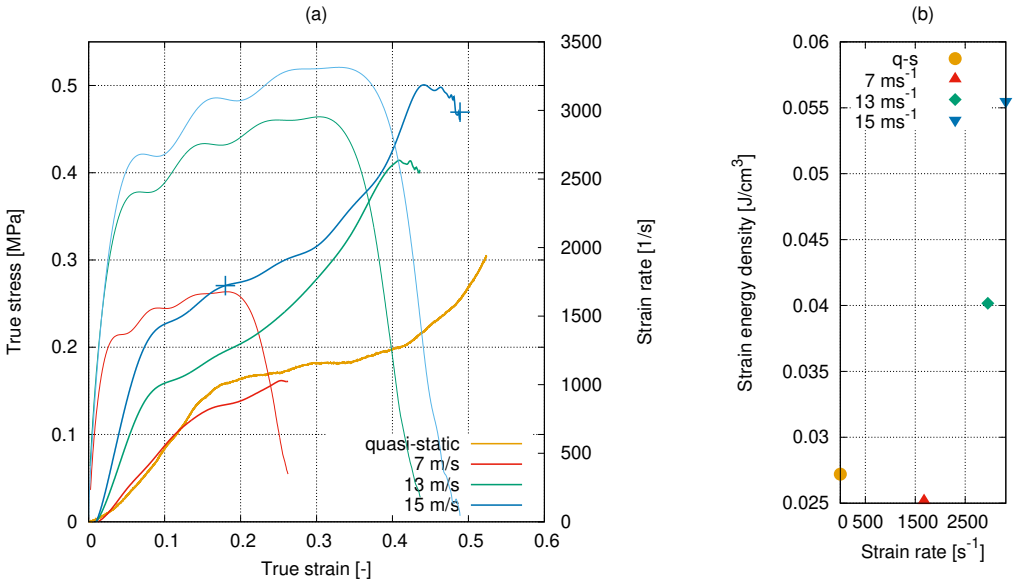

Figure 5.3: Results of the SHPB impact tests of the polyurethane foam.

The results of the tests of the polyurethane foam specimens showed a strain-rate sensitive response in terms of the plateau stress and peak stress at strain-rates higher than 2000 s^{-1}. At the lower strain-rate, the stress-strain curve is of similar shape as the quasi-static response. The value the of strain energy density measured at a strain-rate of 1500 s^{-1} is comparable (even slightly lower) with the value measured at the quasi-static test. Above this strain-rate, the strain energy density increases with an increasing strain-rate.

The calculated strain energy density increases among the series of the SHPB impact tests, however at the lowest strain-rate of 1500 s^{-1}, the value is lower than the value obtained from the quasi-static testing.

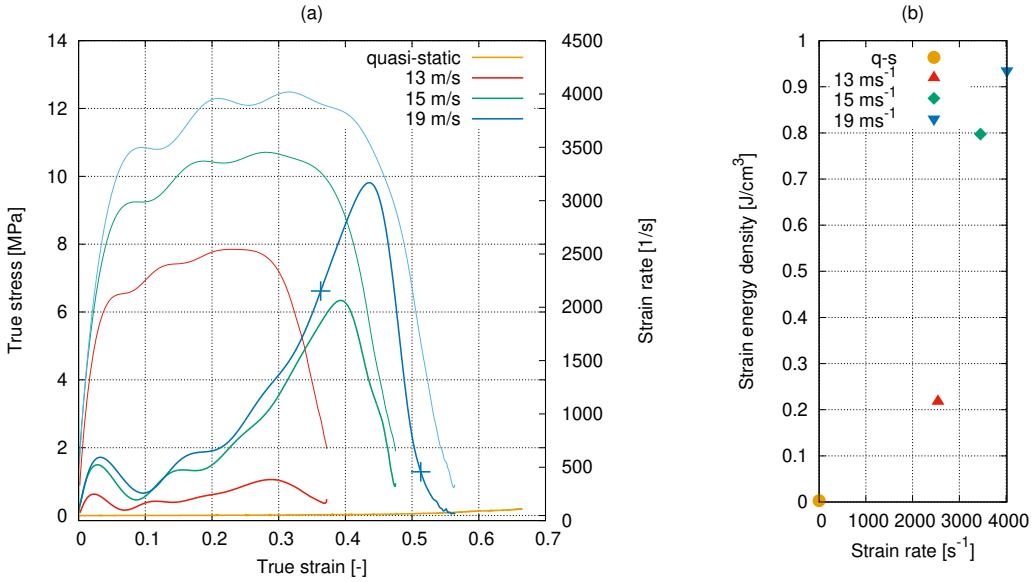

Figure 5.4: Results of the SHPB impact tests of the ordnance gelatin.

The stress-strain curves measured in the series of SHPB test of the ordnance gelatin specimens show a strong strain-rate sensitivity. The plateau stress observed at the lowest strain-rate of the SHPB tests, appprox. 2000 s^{-1}, was 10 times higher in comparison with the quasi-static response. The plateau stress, peak stress as well as the strain energy density also increase strongly with an increasing strain-rate among the series of the SHPB tests. A direct comparison with the impact tests is not possible, as these results (presented in Section 4.2) showed sensitivity not only to the strain-rate, but also on impact energy, which differs significantly between the drop tests and the SHPB.

The stress-strain curves obtained from the tests of the polyurethane putty

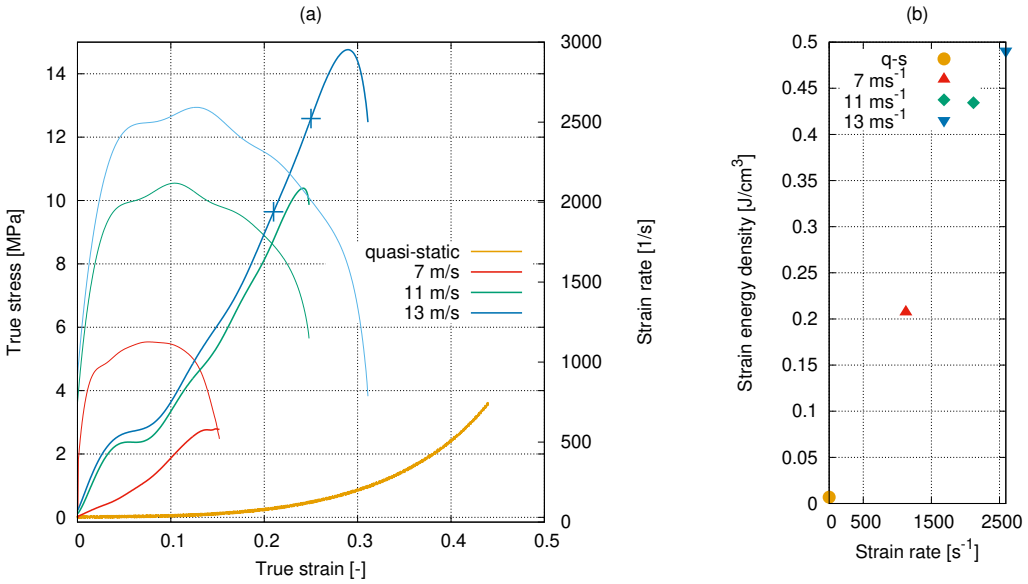

Figure 5.5: Results of the SHPB impact tests of the polyurethane putty.

specimens show a strain-rate sensitive response in the entire range of the tested strain-rates. The response to the SHPB impact contains a very short plateau region before the curves return to a steady increase of stress. The quasi static response exhibita s steady increase in stress over the entire loading curve.

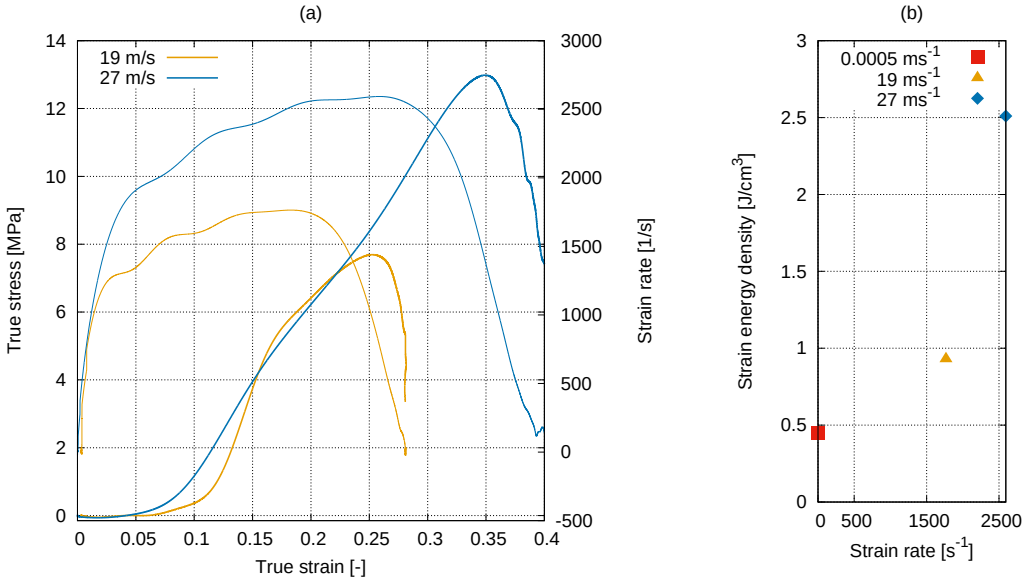

Figure 5.6: Results of the SHPB impact tests of the IPC.

The results of the impact tests of IPC obtained from the open-cell alu-

minium foam and polyurethane putty show an enhanced strain energy density absorption with the highest strain-rate ($1200\,s^{-1}$). The strain-rate sensitivity is detectable over the entire range of the tested strain-rates from the quasi static compression and drop tests to the SHPB impact loading. The constant stress at nearly zero value up to a strain of 0.05 indicates issues with the specimens' shape (precision), which is demonstrated by the short region of settlement.

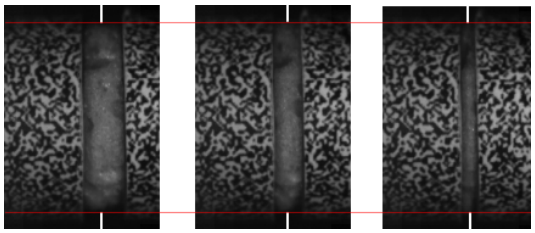

(a) polyurethane foam

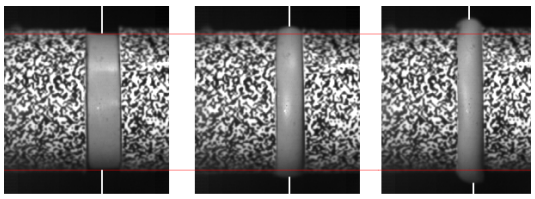

(b) polyurethane putty

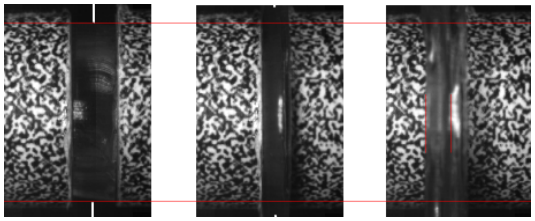

(c) ordnance gelatin

Figure 5.7: Comparison of the intact and deformed state of the filling materials' specimens under impact loading.

The characteristics of the samples' deformation and failure were evaluated using the high-speed camera images. The comparison between the intact and the damaged state of the selected specimens in all three groups are shown in Figure 5.7. The specimens of the polyurethane foam exhibit no significant radial expansion in the plateau region, which corresponds to its porous nature and crushing of the pores during the plateau. On the other hand, the radial expansion of the polyurethane putty specimens is clearly detectable during the entire deformation evolution, which corresponds to the steady increase in stress

without a significant plateau. The specimens of the ordnance gelatin exhibit a slight radial expansion in the initial phase of the tests and subsequently, a failure may be identified at the surface, the development of which occurs in the plateau phase of the stress-strain curves.

5.4 Concluding remarks

Based on the comparative measurement, the response to the compressive loading of the three types of filling material and one representative of IPC was evaluated. The obtained stress-strain curves were analysed together with the sets of images of the intact deforming specimen during the high strain-rate loading. The behaviour corresponds to the measured curves. From the measured stress-strain curves, the strain energy density was calculated for each level of strain-rate in all groups. The results show a significant strain-rate sensitivity of the ordnance gelatin, the polyurethane putty as well as in the IPC over the entire tested range of the strain-rates. The strain-rate effect in the polyurethane foam occurred starting at strain-rates higher than $1500\,\mathrm{s}^{-1}$.

Chapter 6

Auxetic structures: towards higher impact energy absorption

Aside the aforementioned ways to enhance the strain energy absorption capabilities, other possibilities are under investigation at our workplace concerning the impact energy absorption. Among them, auxetics particularly pose a wide range of favourable properties. There are several ways to enhance the energy absorption capabilities of auxetics, the representatives of two such techniques are presented here: (i) the structural optimisation of a 3D inverted honeycomb structure by the controlled stiffness of the struts' joints and (ii) the influence of filling materials on the deformation behaviour of different types of auxetics. Such structures were tested and the results reported in our papers [104, 107, 108].

6.1 Effect of joint stiffness

The mechanical characteristics of auxetics are given not only by the overall geometrical arrangement of struts in the unit cell and their connectivity, but also by the deformation properties of the strut joints. There are two main mechanisms of lattice behaviour during mechanical deformation. Based on the struts' connectivity, the deformation is stretching-dominated for lattices which comply with truss assumptions or bending-dominated in lattices with incomplete connectivity [109]. Hence, the deformation and energy absorption properties are highly influenced by the stiffness of the joints (struts' connections). The influence of all these factors on the effective mechanical properties in both elastic and plastic regime has to be thoroughly evaluated and taken

Specimen height [mm]	26
Specimen cross-section [mm]	16.5×16.5
Number of unit cells	$3 \times 3 \times 3$
Strut cross-section [mm]	0.75×0.75

Table 6.1: Design parameters - common parameters.

into account in an analytical and numerical optimisation.

We reported (a paper* [108]) on the properties of auxetic structures with the controlled stiffness of strut joints. In this paper, we performed a parametric study on the influence of the strut joint stiffness on the effective deformation response of various auxetic lattices.

6.1.1 Specimen design and manufacturing

Auxetic lattices exhibiting a negative Poisson's ratio were designed in the parametric modeller SolidWorks (Dassault Systémes Corp., France). A three-dimensional inverted honeycomb was selected which exhibits an auxetic behaviour in all three dimensions. The design of the tested auxetic structure was based on our previous study [110], in which the first preliminary results were presented. Only entirely auxetic structures were used in contrast to planar auxetics. The porosity and ratio between the cell size and strut cross-section (square shaped) was accommodated to obtain a better stiffness and strength. At the top and bottom plane, a plate was added in to ensure a better force transfer between the loading grips and the specimens. The design parameters of the specimens are listed in Table 6.1, the geometry of the unit cell is depicted in Figure 6.1.

Different joint stiffness was achieved by differently sized spheres placed in the intersections of the struts. Three different radii were selected. Upper limit value of the spheres' radius (1.875 mm) was selected to avoid contact between neighbouring spheres. The lower limit (0.938 mm) was selected with respect to a possible observation of the reinforcing effect, as smaller spheres would be entirely hidden in the intersection of the prismatic struts. Parameters of the

*T. Doktor, T. Fíla, P. Koudelka, D. Kytýř, and O. Jiroušek. Compressive properties of auxetic structures with controlled stiffness of strut joints. In *17th Youth Symposium on Experimental Solid Mechanics*, YSESM 2019, volume 25 of Acta Polytechnica CTU Proceedings, pages 17–20, 2019.

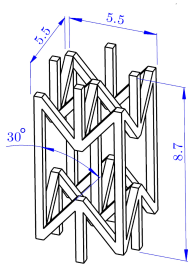

Figure 6.1: Geometry of the used auxetic unit cell.

Group	Sphere radius [mm]	Porosity [%]
0	-	78.8
1	0.75	76.9
2	0.9375	72.4
3	1.125	64.9

Table 6.2: Design parameters - joint reinforcement variations.

joints' reinforcement are listed in Table 6.2.

The STL models which were used for the 3D printing of the tested samples are depicted in Figure 6.2.

The specimens were manufactured by direct 3D printing from a UV-curable acrylic material VisiJet EX200 (3D Systems, USA) using a Pro Jet HD3000 3D printer (3D Systems, USA) in high definition mode. The resolution in high definition mode was $387 \times 387 \times 300$ dpi.

6.1.2 Compression tests

For the compression experiments, a custom loading device was used equipped with a force transducer with a loading capacity of 2 kN (U9b, Hottinger Baldwin Messtechnik GmbH, Germany). The loading was provided by a stepper motor controlled by a LinuxCNC software solution used with a real-time GNU/Linux operating system [101]. The tests were displacement driven with a loading rate of $20\mu m \cdot s^{-1}$. A contactless displacement measurement was employed based on digital image correlation (DIC) [51, 52]. The loading scene was captured by a CCD camera (Manta G504B, Alied Vision Technologies GmbH, Germany) attached to a bi-telecentric zoom lens (TZCR 072, OptoEngineering, Italy). The image date was captured with a custom software tool based on the OpenCV library [94]. A zoom ratio of $0.25\times$ was used for all the compressive

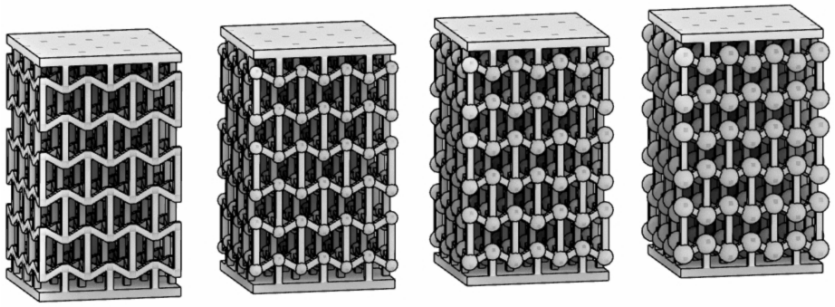

Figure 6.2: STL models for 3d printing.

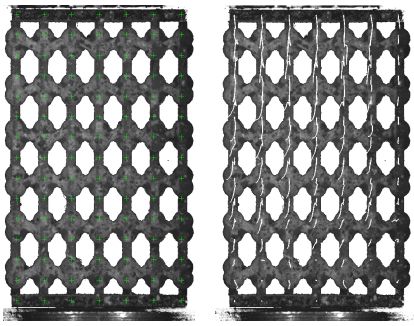

Figure 6.3: Loading scene with tracking features (left) and tracked displacement paths (right). Black background was inverted due to a better visibility.

tests, which provided a pixel-size of 13.7 μm. A set of tracking features was selected in the first (undeformed) loading scene which were arranged into 7 columns and 15 rows to ensure the placement of the features in the solid material of the struts. The array of loading features is depicted in Figure 6.3 (left). The loading rate together with the frame rate of 2 fps ensured a sufficient number of points in the obtained loading curve. Figure 6.3 (right) shows the displacement paths tracked by DIC in the selected specimen from group 2.

The measured displacements and forces were used to calculate the engineering strain ε_{eng} and stress σ_{eng} which were converted into the true strain ε_{true} and true stress σ_{true} using Equations (3.5) and (3.6), respectively.

Based on the measured strain in transversal and longitudinal direction, Poisson's ratio was calculated according to Equation (6.1).

$$\mu = -\frac{\varepsilon_x}{\varepsilon_y} \tag{6.1}$$

To exclude values which correspond to both the initial settlement and post-yield region after the first plastic collapse, the function of Poisson's ratio was limited only inside these limit values of the strain. Moreover, to assess the

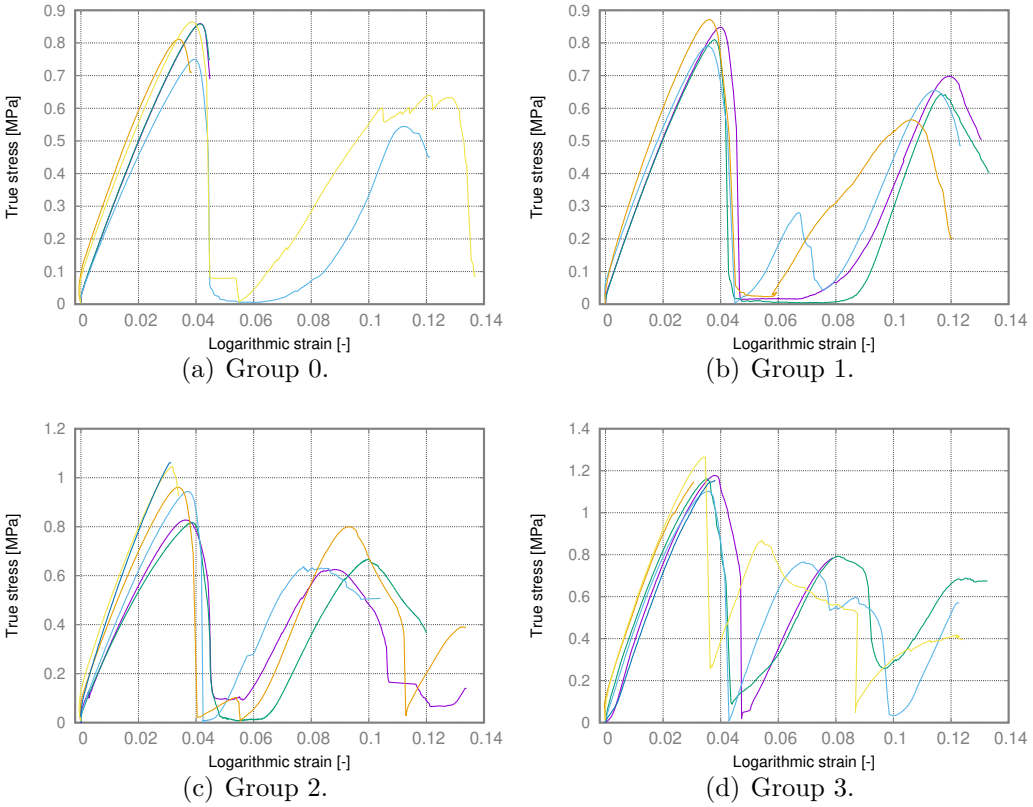

(a) Group 0. (b) Group 1.

(c) Group 2. (d) Group 3.

Figure 6.4: Stress-strain curves of the 3D re-entrant specimens with the different reinforcement in the struts' joints.

influence of the joints' stiffness on the mechanical behaviour, the ultimate compressive stress of the tested structures was evaluated as well as the strain corresponding to the first plastic collapse.

6.1.3 Results

A series of uniaxial compressive tests was performed on custom designed three-dimensional inverted honeycomb structures. From the captured loading scenes, the evolution of the deformation of the tested structures is assessed. The true stress vs. logarithmic strain diagrams are depicted in Figure 6.4 for groups 0 to 3. In all the groups, the stress strain curves start with a linear part, which is followed by a sudden drop. This represents a collapse of one of the layers of the auxetic unit cells. This is caused by the high brittleness of the base material. After the collapse, the loading continued with a similar stress-strain behaviour, but with slightly lower stresses at the consequent collapses.

Group	σ_m [MPa]	ε_{y1} [1]	μ_{mean} [1]
0	0.876 ± 0.124	0.0383 ± 0.0032	-0.180 ± 0.040
1	0.887 ± 0.134	0.0348 ± 0.0029	-0.219 ± 0.058
2	0.942 ± 0.138	0.0346 ± 0.0030	-0.142 ± 0.030
3	1.168 ± 0.054	0.0352 ± 0.0027	-0.047 ± 0.065

Table 6.3: Average results in the tested groups. The stress and strain at the first collapse. Average Poisson's number.

To compare the main mechanical properties of the tested structures and to assess the influence of the different reinforcement of the strut joints, the mean values among the groups were evaluated with their standard deviations. In Table 6.3, the mean ultimate compressive strength (the stress at the first collapse), the strains corresponding to the first collapse in each group of the samples and the mean values of Poisson's ratio in the region up to the first collapse are listed.

6.1.4 Concluding remarks

An experimental study on the deformation response of 3D printed auxetic structures was carried out to evaluate the influence of the joint properties which were physically simulated by adding an extra amount of material in the struts' connections. The loading setup was equipped with a custom contactless strain measurement system which enabled the precise evaluation of the stress-strain curve. The obtained curves exhibited consistent behaviour among each group (i.e. sphere radius) in terms of the stiffness in the linear part, the ultimate compressive strength and the strain at the first collapse.
The stress level at the first collapse increases with the increasing stiffness in the joints, while the strain at the first collapse remains unchanged. The auxetic nature exhibits slight a increase when the spheres with the lowest radii are added in the joints' interconnections. Then, with the increasing spheres' radius, the auxetic behaviour is less significant. This experimental campaign showed the high influence of the stiffness in the struts' interconnections. The additive manufacturing techniques together with the numerical optimisation also allow for other promising ways of inexpensive optimisation, based, e.g., on a change in the struts' geometry along their axes. This would allow for structures with a highly optimised stiffness with unique properties.

Moreover, on the effect of the joints' stiffness in the re-entrant structures, a numerical study was performed based on the experimetal results presented hereinbefore[†] [107]. In the study, the stress concentrations in the auxetics' struts were analysed and more uniform the stress distributions was confirmed in the case of the reinforced struts' joints. Nevertheless, the numerical analyses are beyond the scope of this dissertation, but they are comprehensively studied in the dissertation of Petr Koudelka [111].

6.2 Effect of filling

To assess the effect of the filling materials under higher strain-rate impact loading, a series of auxetic, additively manufactured, structures were tested at strain-rates varying from $2000\,\mathrm{s}^{-1}$ to $2800\,\mathrm{s}^{-1}$. The effect of each considered filling on the impact response characteristics (plateau stress and strain energy density) was assessed. From the images of the deforming loading scene captured using a high speed camera, the strain fields were obtained and the effect of the filling on Poisson's ratio was evaluated. The investigations and results presented in this section were partially published in our paper[‡] [104].

6.2.1 Specimens' design and manufacturing

For this experimental campaign, three types of auxetics were designed and produced by selective laser sintering (SLS), two of which exhibited an in-plane auxetic behaviour, while the third structure posed negative Poisson's ratio in three dimensions: (i) a missing rib (cross-chiral) structure, (ii) a 2D re-entrant (inverted honeycomb) and (iii) a fully re-entrant structure. The used lattices are depicted in Figure 6.5. These representatives of auxetics were selected based on the capabilities of the SLS to produce the samples with satisfactory resolution and with reasonable dimensions of the unit cell. As the overall dimensions are limited by the design parameters of the used SHPB, only 3-by-3

[†] **T. Doktor**, T. Fíla, P. Koudelka, D. Kytýř, and O. Jiroušek. Compressive properties of auxetic structures with controlled stiffness of strut joints. In *17th Youth Symposium on Experimental Solid Mechanics*, YSESM 2019, volume 25 of Acta Polytechnica CTU Proceedings, pages 17–20, 2019.

[‡] T. Fíla, P. Zlámal, O. Jiroušek, J. Falta, P. Koudelka, D. Kytýř, **T. Doktor**, and J. Valach. Impact testing of polymer-filled auxetics using split Hopkinson pressure bar. *Advanced Engineering Materials*, 19(10):1–13, 2017.

	horizontal direction	vertical direction
compressive strength [MPa]	574 ± 10	662 ± 2
yield strength [MPa]	518 ± 5	440 ± 10
Young's modulus [GPa]	167 ± 8	134 ± 17

Table 6.4: Mechanical properties of the base material for the SLS (316L-0407 alloy)

(or, in the case of three-dimensionally auxetic structure 3-by-3-by-3) might be used, which enabled one unit cell without direct connection to the samples' endplate which was used for load transfer purposes.

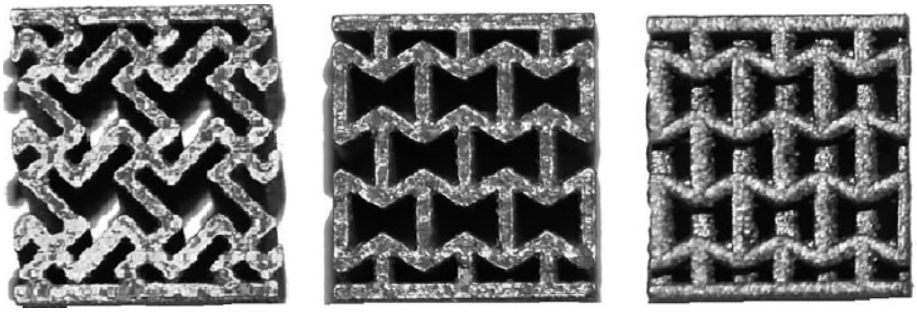

(a) missing rib (b) 2D re-entrant (c) 3D re-entrant

Figure 6.5: Samples of auxetics tested with fillings (SLS printed)

The dimension of the designed samples of the missing rib, 2D re-entrant and 3D re-entrant were (w × d × h) were 11.7 × 12.0 × 13.0 mm and 11.7 × 12.0 × 13.0 mm and 11.7 × 12.0 × 13.0 mm, respectively. The nominal values of porosity were 53.1 %, 52.3 % and 74.0 %, respectively.

The samples were manufactured by SLS from an austenitic stainless steel alloy 316L-0407 (an extra low carbon alternative to 316L alloy). The density of the base material is 7990 kg m^{-3}, the melting point varies between $1371 - 1399\,°C$. The mechanical properties in both horizontal and vertical direction are listed in Table 6.4.

To assess the effect of the filling materials on the mechanical response at high strain-rates, the manufactured samples were then divided into three groups: (i) unfilled group, (ii) filled with a polyurethane foam and (iii) filled with an ordnance gelatin. The properties and preparation procedure of the fillings are described in detail in Section 3.4. The resulting density of each sample group, evaluated after the filling process, is listed in Table 6.5. These values

ρ[kg m^{-3}]	unfilled	polyurethane foam	ordnance gelatin
missing rib	4266	4415	4845
2D re-entrant	4381	4456	4976
3D re-entrant	2944	3041	3686

Table 6.5: Density of the polymer-filled auxetics

were subsequently used to obtain the values of the strain energy absorbed per kilogram.

6.2.2 Quasi-static tests

From each of the 9 groups (three structures × three groups of filling options), one sample was selected for the quasi-static testing. An Instron 3382 uniaxial loading machine (Instron, USA) was used for the displacement controlled compression. The loading rate was $0.5\,\mathrm{mm}\cdot\mathrm{s}^{-1}$ which resulted in a strain-rate of $0.0011\,\mathrm{s}^{-1}$. The loading was conducted up to 50 % of the overall strain. For the further evaluation of the strain field, the loading scene was captured using a digital camera attached to a telecentric lens. In the acquired images, the displacements were tracked by DIC and then, the in-plane strains were calculated.

6.2.3 SHPB tests

The tests at high strain-rates were performed using an SHPB apparatus based on Kolsky setup. The instrumentation and procedure did not differ from the campaign presented in Section 5.2, except the material of the striker, incident and transmission bars. As the tested samples manufactured from steel exhibited higher mechanical impedance, aluminium bars were used in this series of experiments. To adjust the shape of the strain pulses generated in the incident bar and reduce the wave dispersion, pulse shapers were used. Based on the calibration experiments performed prior to this campaign, paper pulse-shapers were used (thickness $2 \times 0.25\,\mathrm{mm}$), which allowed one to achieve nearly constant strain-rates in the plateau regions. All the tests were performed with a unchanged level of a gas gun release pressure of 5 bar. The resulting impact velocity of the striker bar was $33\,\mathrm{m}\cdot\mathrm{s}^{-1}$.

6.2.4 Evaluation

The measured strain gauge signals were evaluated according to the 1-dimensional wave propagation theory in elastic media. The equations describing the waves, presented in Section 2.3.2, are implemented by an in-house software [106], which allows one to obtain the stress-strain curves as well as the strain-rate-strain dependencies. From the stress-strain curves, the strain energy density was calculated according to Equation 4.2. To evaluate the effect of the filling on the auxetic behaviour, Poisson's function was calculated using Equation 6.1 based on the longitudinal and transversal strains obtained by DIC.

6.2.5 Results

Based on the strain signals measured on the SHPB, the stress-strain curves were obtained. These curves, for all three types of auxetics are presented in Figures 6.6–6.8, together with the comparison of the values of the strain energy density calculated for both the quasi-static loading and SHPB impacts.

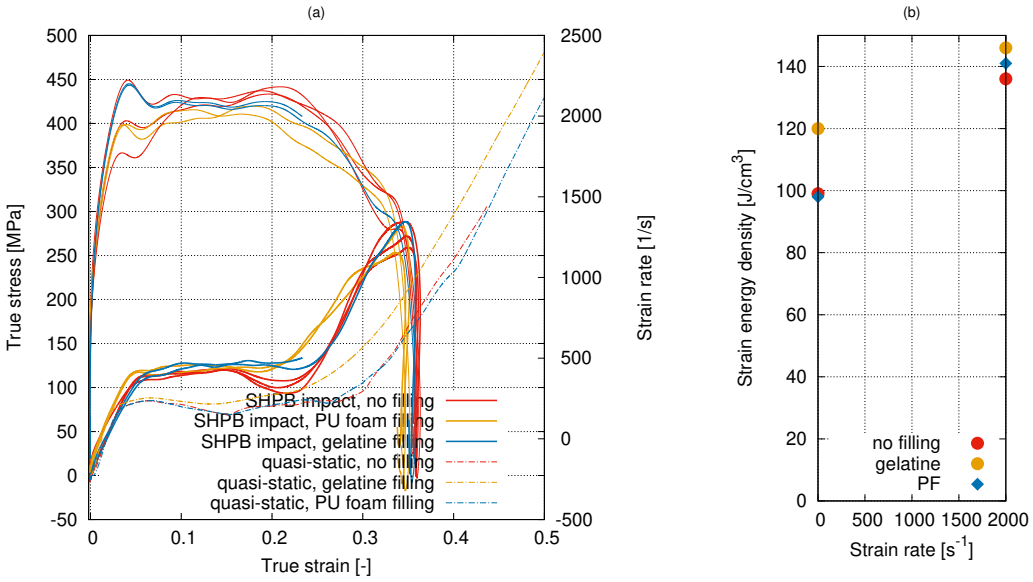

Figure 6.6: Results of the SHPB impact tests of the 2D re-entrant structure - comparison of the filled and unfilled samples

In the obtained stress-strain curves, a clearly detectable plateau region is present starting at 15% of the strain in all three types of tested auxetics and reaching up to 25%, 25% and 15% strain in the 2D re-entrant, 3D re-entrant

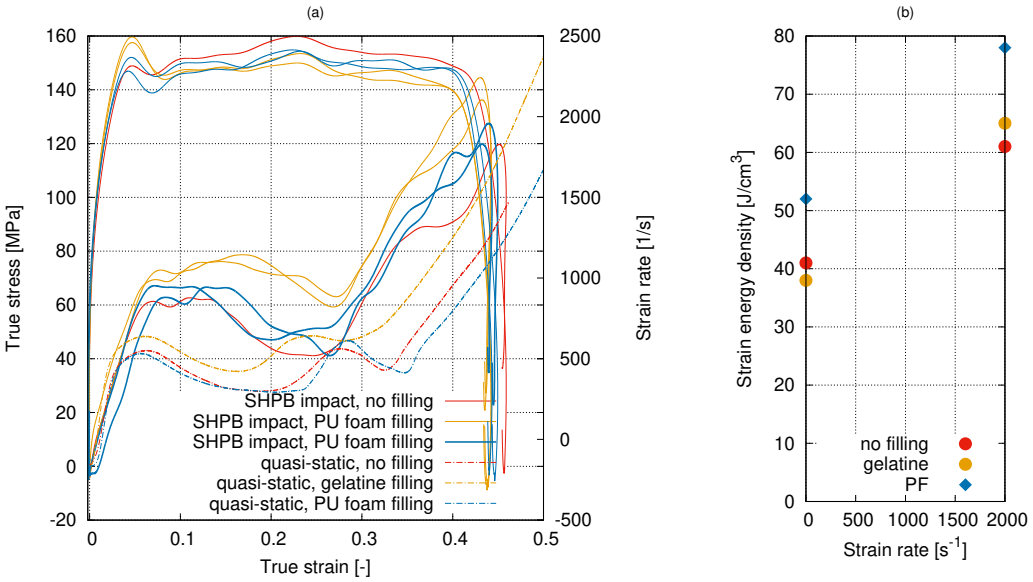

Figure 6.7: Results of the SHPB impact tests of the 3D re-entrant structure - comparison of the filled and unfilled samples

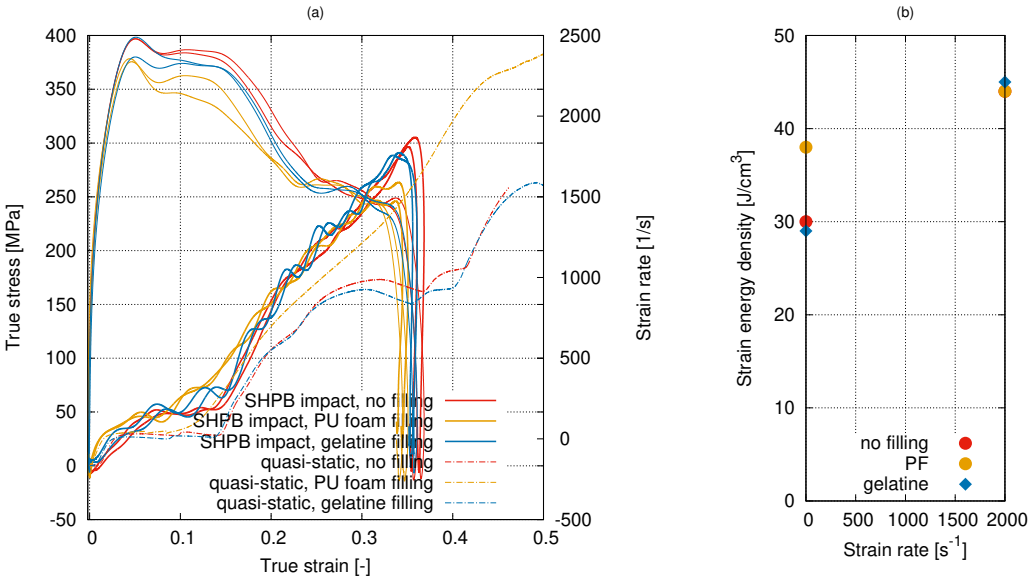

Figure 6.8: Results of the SHPB impact tests of the 2D missing rib structure - comparison of the filled and unfilled samples

and 2D missing rib, respectively. The plateau stress values as well as the comparison of the absorbed energy among the tested groups of auxetics with different filling materials are presented in Table 6.6.

Based on the image data recorded by the high-speed camera during the

	Average plateau stres			Specific energy ratio	Filling energy effect ratio	
	Static	Dynamic	Ratio	Dynamic vs. Static	Static	Dynamic
2D re-entrant						
Unfilled	80 MPa	113 MPa	1.41	1.43	-	-
PF	85 MPa	121 MPa	1.42	1.42	1.09	1.06
Gelatin	79 MPa	123 MPa	1.53	1.58	1.00	1.11
3D re-entrant						
Unfilled	33 MPa	51 MPa	1.56	1.55	-	-
PF	40 MPa	72 MPa	1.73	1.71	1.27	1.37
Gelatin	31 MPa	56 MPa	1.70	1.78	0.96	1.09
missing rib						
Unfilled	30 MPa	49 MPa	1.66	1.66	-	-
PF	34 MPa	57 MPa	1.69	1.70	1.15	1.18
Gelatin	28 MPa	52 MPa	1.76	1.95	0.90	1.06

Table 6.6: Comparison of the plateau stress and strain energy density for the filled auxetic samples

SHPB tests, the strains were calculated using DIC. The obtained Poisson's function for each type of auxetic structure is depicted in Figures 6.9–6.11. Due to the small values of the strain in the initial phase of the impact loading, Poisson's ratio corresponding to of the first two images differs significantly even in the same groups of samples. However, after this initial phase, the calculated Poisson's function started to be consistent among each group.

In the unfilled samples of the 2D re-entrant structure, Poisson's ratio increases steadily from -0.3 at a 1% strain to -0.08 at a 35% strain. In the samples of the same structure filled with polyurethane foam and ordnance gelatin, the displayed Poisson's ends with a lower strain value. This was determined by the presence of the filling in the loading scene, which, at higher levels of compression, caused strong changes at the samples' surface and a loss of correlation in the optical strain measurement. In the 2D re-entrant samples filled with the polyurethane foam, Poisson's ratio steadily increases from -0.08 at a 1% strain to 0.08 at a 18% strain, while the zero value of Poission's ratio is reached at a 15% strain. In the 2D re-entrant samples, Poisson's ratio increases

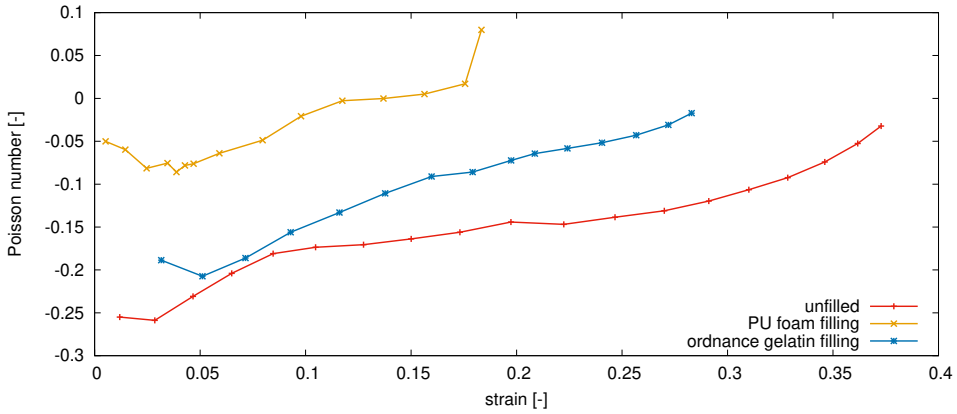

Figure 6.9: Poisson's function measured in the group of 2D re-entrant specimens.

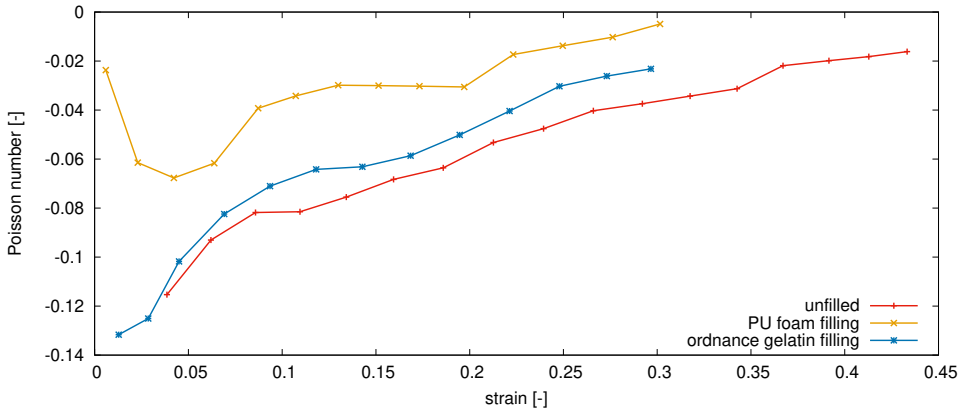

Figure 6.10: Poisson's function measured in the group of 3D re-entrant specimens.

steadily from -0.2 at a 1% strain to 0 at a 30% strain.

In the group of 3D re-entrant samples, Poisson's ratio preserves the negative sign up to a 30% strain. In the unfilled samples and the samples filled with ordnance gelatin, Poisson's function exhibits a steady increase, where Poisson's ratio of the unfilled samples is slightly lower. In the samples filled with polyurethane foam, a slight decrease from -0.02 at a 1% strain to -0.07 at 5% strain occurs followed by an increase to -0.005 at a 30% strain.

In the group of 2D missing rib samples, Poission's function increases for the unfilled samples as well as for both types of filling and, in all cases, reaches the zero value of Poission's ratio at strains of 0.25, 0.18 and 0.15 for the unfilled samples, polyurethane foam filling and ordnance gelatin filling, respectively.

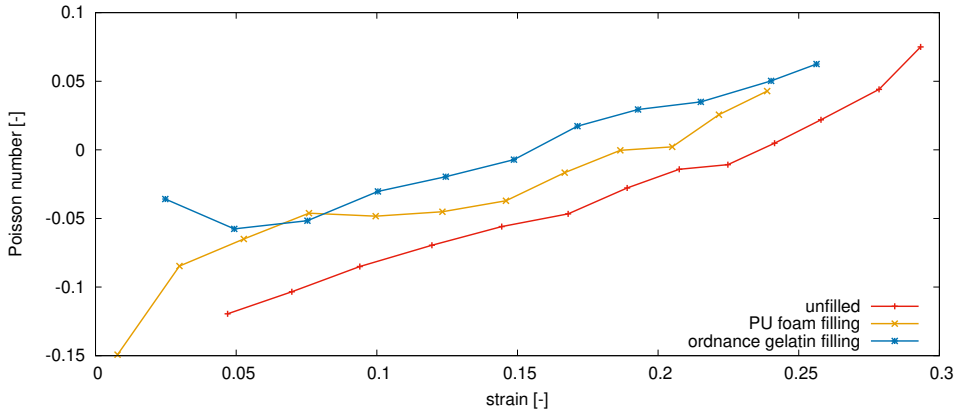

Figure 6.11: Poisson's function measured in the group of missing rib specimens.

6.2.6 Concluding remarks

Three types of additively manufactured auxetics, 2D and 3D re-entrant structure and 2D missing rib structure were tested at quasi-static and high strain-rate conditions in a compression mode. The influence of two types of filling materials on the energy absorption properties were evaluated as well as the influence on the auxetic behaviour of these lattices. The obtained results at a quasi-static strain-rate show a positive influence on the strain energy density when the polyurethane foam filling was used, while the influence of the ordnance gelatin was negligible. At a strain-rate of $2000\,\mathrm{s}^{-1}$, an increase in the absorbed impact energy was observed for both types of filling. Moreover, the influence of the filling on the auxetic behaviour was evaluated using an optical strain measurement. For both types of filling, the auxetic nature was slightly suppressed at high strain-rates.

Chapter 7

Summary

This thesis was focused on the investigations into the different possibilities to tune and enhance the impact energy absorption properties of cellular materials. For this purpose, representatives of cellular metallic structures were tested together with representatives of polymeric materials used as fillers to form IPCs. The investigated types of materials were tested at different scale levels for the description of the structural properties and mechanical response of the base material. To assess the energy absorption properties of the selected types of materials, the tests were performed at different strain-rates: quasi-static loading, moderate strain-rate impacts (dozens of s^{-1}) using a drop tower and higher strain-rate impacts using an SHPB apparatus, reaching strain-rates of lower thousands of s^{-1}. Based on the results of the performed experimental campaigns, several conclusions may be highlighted:

- The experimental campaigns carried out at moderate strain-rates using a drop tower showed a strain-rate sensitive response at moderate strain-rates in the ordnance gelatin and IPC, while the response of unfilled aluminium foam remained unchanged with an increasing strain-rate. In the ordnance gelatin, the response also depended on the impact energy, even at the same impact velocity.

- The high strain-rate impact using the SHPB showed a strain-rate sensitivity in the impact energy absorption characteristics (plateau stress, strain energy density) for all the tested materials (polyurethane foam, ordnance gelatin, polyurethane putty, IPC).

- The high strain-rate impact tests confirmed the positive influence of both types of tested filling (polyurethane foam, ordnance gelatin) on energy absorption capabilities of the additively manufactured auxetics.
- The optical strain measurement of the SHPB impact tests of the polymer-filled auxetics showed a reduction in the auxetic nature with the presence of the filling.

The experimental campaigns with their results presented in this thesis, were published in several peer-reviewed journals or proceedings papers (see Appendix A). These results were part of the outputs of the research projects supported by Czech Science Foundation: (i) project No. P105/12/0824 entitled "Determination of Structural and Mechanical Properties of Metal Foams Using Nanoindentation, Computer tomography and Microstructural FEM models" and (ii) project No. 15-15480S entitled "Optimized auxetic structures for cellular metals filled with strain-rate sensitive material for high velocity impacts" with a total budget of €321 000 and €213 000, respectively. The projects were finished and evaluated as successfully solved. Moreover, project No. P105/12/0824 was evaluated as excellent showing exceptional results with an international impact.

Bibliography

[1] G. H. Waltz Jr. Making the Dead seat safer. *Popular Science*, pages 82–89, July 1950.

[2] U. Seiffert. *Automotive safety handbook*. SAE International Professional Engineering Pub, Warrendale, Pa. London, UK, 2003.

[3] R. Juntikka and S. Hallström. Selection of energy absorbing materials for automotive head impact countermeasures. *Cellular Polymers*, 23(5):263–298, 2004.

[4] M. Peden, editor. *World report on road traffic injury prevention*. World Health Organization, Geneva, CH, 2004.

[5] T. Ngo, C. Ding, R. Lumantarna, A. Ghazlan, and M. Zobec. Structural performance of double-skin façade systems subjected to blast pressures. *Journal of Structural Engineering (United States)*, 141(12), 2015.

[6] D. Yongxiang, F. Shunshan, X. Changjing, and G. Lele. Dynamic behaviour of concrete sandwich panel under blast loading. *Defence Science Journal*, 59(1):22–29, 2009.

[7] M. M. A. Wahab and S. A. Mazek. Performance of double reinforced concrete panel against blast hazard. *Computers and Concrete*, 18(4):807–826, 2016.

[8] H. P. Degischer and B. Kriszt. *Handbook of cellular metals: Production, Processing, Applications*. Wiley, 2002.

[9] J. Kwon and G. Subhash. Compressive strain rate sensitivity of ballistic gelatin. *Journal of Biomechanics*, 43(3):420–425, 2010.

[10] ERG Aerospace Corporation. Duocel foam energy absorbtion. available from: http://www.ergaerospace.com/Energy-Absorbtion.html.

[11] B. Song, W. Chen, S. Dou, N. Winfree, and J. Kang. Strain-rate effects on elastic and early cell-collapse responses of a polystyrene foam. *International Journal of Impact Engineering - INT J IMPACT ENG*, 31:509–521, 05 2005.

[12] K. A. Dannemann and J. Lankford Jr. High strain rate compression of closed-cell aluminum foams. *Materials Science and Engineering A*, 293(1):157–164, 2000.

[13] A. Paul and U. Ramamurty. Strain rate sensitivity of a closed-cell aluminum foam. *Materials Science and Engineering: A*, 281:1–7, 04 2000.

[14] R. Goldberg. Strain rate dependent deformation and strength modeling of a polymer matrix composite utilizing a micromechanics approach. In *NASA/TM—1999-209768*, 01 2000.

[15] W. J. Kang and H. Huh. Crash analysis of auto-body structures considering the strain-rate hardening effect. In *Seoul 2000 FISITA World Automotive Congress*. Society of Automotive Engineers of Korea, jun 2000.

[16] M. Shkolnikov. Strain rates in crashworthiness. In *8th International LS-Dyna Users Conference*, pages 1–9, 01 2004.

[17] L. J. Gibson and M. F. Ashby. *Cellular Solids: Structure and Properties*. Cambridge Solid State Science Series. Cambridge University Press, 2 edition, 1997.

[18] B. Sosnik, 1948. US patent No. 2 434 775.

[19] J. C. Elliot, 1956. US patent No. 2 751 289.

[20] J. Banhart. Manufacture, characterisation and application of cellular metals and metal foams. *Progress in Materials Science*, 46(6):559–632, 2001.

[21] C. Kammer. Aluminium foam. In *Training in Aluminium Application Technology*. European Aluminium Association, 1999.

[22] Q. Chen and N. M. Pungo. In-plane elastic buckling of hierarchical honeycomb materials. *European Journal of Mechanics A/Solids*, 34:120–129, 2012.

[23] R. Harb, E. Taciroglu, and N. Ghoniem. Partitioning of elastic energy in open-cell foams under finite deformations. *Acta Materialia*, 61(5):1454–1468, 2013.

[24] W. Chen, F. Lu, and N. Winfree. High-strain-rate compressive behavior of a rigid polyurethane foam with various densities. *Experimental Mechanics*, 42(1):65–73, 2002.

[25] W. Chen, F. Lu, D. J. Frew, and M. J. Forrestal. Dynamic compression testing of soft materials. *Journal of Applied Mechanics, Transactions ASME*, 69(3):214–223, 2002.

[26] L. Zhang, M. Gurao, K. H. Yang, and A. I. King. Material characterization and computer model simulation of low density polyurethane foam used in a rodent traumatic brain injury model. *Journal of Neuroscience Methods*, 198(1):93–98, 2011.

[27] Y. Sugimura, J. Meyer, M. Y. He, H. Bart-Smith, J. Grenstedt, and A. G. Evans. On the mechanical performance of closed cell Al alloy foams. *Acta Materialia*, 45(12):5245–5259, 1997.

[28] X. Zheng, H. Lee, T. H. Weisgraber, M. Shusteff, J. DeOtte, E. B. Duoss, J. D. Kuntz, M. M. Biener, Q. Ge, J. A. Jackson, S. O. Kucheyev, N. X. Fang, and C. M. Spadaccini. Ultralight, ultrastiff mechanical metamaterials. *Science*, 344(6190):1373–1377, 2014.

[29] X. Yan and P. Gu. A review of rapid prototyping technologies and systems. *Computer-Aided Design*, 28(4):307 – 318, 1996.

[30] M. Shellabear and O. Nyrhilä. DMLS-Development history and state of the art. *Proceedings of the 4th LANE 2004, Sept. 22.-24*, 01 2004.

[31] A. Jung, H. Natter, R. Hempelmann, S. Diebels, and E. Lach. Improved mechanical properties of nano-nickel strengthened open cell metal foams. In *Society for Experimental Mechanics - SEM Annual Conference and Exposition on Experimental and Applied Mechanics 2010*, volume 1, pages 340–344, 2010.

[32] A. Jung, H. Natter, R. Hempelmann, S. Diebels, R. Koblischka, U. Hartmann, and E. Lach. Study of the magnetic flux density distribution of nickel coated aluminum foams. *Journal of Physics: Conference Series*, 200(SECTION 8), 2010.

[33] A. Jung, H. Natter, R. Hempelmann, and E. Lach. Nanocrystalline alumina dispersed in nanocrystalline nickel: Enhanced mechanical properties. *Journal of Materials Science*, 44(11):2725–2735, 2009.

[34] A. S. Dalaq, D. W. Abueidda, R. K. Abu Al-Rub, and I. M. Jasiuk. Finite element prediction of effective elastic properties of interpenetrating phase composites with architectured 3D sheet reinforcements. *International Journal of Solids and Structures*, 83:169 – 182, 2016.

[35] X. L. Gong, Y. Liu, S. Y. He, and J. Lu. Manufacturing and low-velocity impact response of a new composite material: Metal porous polymer composite (mppc). *Journal of Materials Science and Technology*, 20(SUPPL.):65–68, 12 2004.

[36] Y. Liu and X.-L. Gong. Compressive behavior and energy absorption of metal porous polymer composite with interpenetrating network structure. *Transactions of Nonferrous Metals Society of China*, 16:s439–s443, Jun 2006.

[37] N. Dukhan, N. Rayess, and J. Hadley. Characterization of aluminum foam–polypropylene interpenetrating phase composites: Flexural test results. *Mechanics of Materials*, 42:134–141, 02 2010.

[38] C. Periasamy, R. Jhaver, and Hareesh Tippur. Quasi-static and dynamic compression response of a lightweight interpenetrating phase composite foam. *Materials Science and Engineering: A*, 527:2845–2856, 05 2010.

[39] D. D. Luong, D. Pinisetty, and N. Gupta. Compressive properties of closed-cell polyvinyl chloride foams at low and high strain rates: Experimental investigation and critical review of state of the art. *Composites Part B: Engineering*, 44(1):403 – 416, 2013.

[40] R. Lakes. Foam Structures with a Negative Poisson's Ratio. *Science*, 235(4797):1038–1040, 1987.

[41] K. E. Evans. Auxetic polymers: a new range of materials. *Endeavour*, 15(4):170 – 174, 1991.

[42] R. Magalhaes, P. Subramani, T. Lisner, S. Rana, B. Ghiassi, R. Fangueiro, D. V. Oliveira, and P. B. Lourenco. Development, characterization and analysis of auxetic structures from braided composites and study the influence of material and structural parameters. *Composites Part A: Applied Science and Manufacturing*, 87:86–97, 2016.

[43] J. Schwerdtfeger, P. Heinl, R. F. Singer, and C. Körner. Auxetic cellular structures through selective electron-beam melting. *Physica Status Solidi (B) Basic Research*, 247(2):269–272, 2010.

[44] F. Scarpa, J. R. Yates, L. G. Ciffo, and S. Patsias. Dynamic crushing of auxetic open-cell polyurethane foam. *Proceedings of the Institution of Mechanical Engineers, Part C: Journal of Mechanical Engineering Science*, 216(12):1153–1156, 2002.

[45] F. Scarpa, L. G. Ciffo, and J. R. Yates. Dynamic properties of high structural integrity auxetic open cell foam. *Smart Materials and Structures*, 13(1):49–56, nov 2003.

[46] T. C. Lim, A. Alderson, and K. L. Alderson. Experimental studies on the impact properties of auxetic materials. *physica status solidi (b)*, 251(2):307–313, 2014.

[47] W. C. Oliver. An improved technique for determining hardness and elastic modulus using load and displacement sensing indentation experiments. *Journal of Materials Research*, 7(6):1564–1583, 1992.

[48] D. Gianola and C. Eberl. Micro and nanoscale tensile testing of materials. *JOM: the journal of the Minerals, Metals & Materials Society*, 61:24–35, 03 2009.

[49] O. Jiroušek, J. Němeček, D. Kytýř, J. Kunecký, P. Zlámal, and T. Doktor. Nanoindentation of trabecular bone-comparison with uniaxial testing of single trabecula. *Chemicke Listy*, 105(17):s668–s671, 2011.

[50] T. Doktor, O. Jiroušek, D. Kytýř, P. Zlámal, and I. Jandejsek. Real-time X-ray microradiographic imaging and image correlation for local strain mapping in single trabecula under mechanical load. *Journal of Instrumentation*, 6(11), 2011.

[51] B. D. Lucas and T. Kanade. An iterative image registration technique with an application to stereo vision. *In: Proceedings of Imaging Understanding Workshop*, pages 121–130, 1981.

[52] I. Jandejsek, J. Valach, and D. Vavrik. Optimization and calibration of Digital Image Correlation method. In P. Smid, editor, *In: Proceedings of Experimental Stress Analysis 2010*, pages 121–126, 2010.

[53] J. Radon. Über die Bestimmung von Funktionen durch ihre Integralwerte längs gewisser Mannigfaltigkeiten. *Berichte Über Die Verhandlungen der Königlich-Sächsischen Akademie der Wissenschaften zu Leipzig, Mathematisch-Physische Klasse [Reports on the Proceedings of the Royal Saxonian Academy of Sciences at Leipzig, Mathematical and Physical Section]*, 69:262–277, 1917.

[54] J. C. Elliott and S. D. Dover. X-ray microtomography. *Journal of Microscopy*, 126(2):211–213, 1982.

[55] P. Mozzo, C. Procacci, A. Tacconi, P. Tinazzi Martini, and I. A. Bergamo Andreis. A new volumetric CT machine for dental imaging based on the cone-beam technique: Preliminary results. *European Radiology*, 8(9):1558–1564, 1998.

[56] U. Hilpert, M. Bartscher, M. Neugebauer, J. Goebbels, G. Weidemann, and C. Bellon. Simulation-aided computed tomography (CT) for dimensional measurements. In *nternational Symposium on Digital industrial Radiology and Computed Tomography*, pages 1–15, 01 2007.

[57] J. Jakůbek, T. Holý, M. Jakůbek, D. Vavřík, and Z. Vykydal. Experimental system for high resolution X-ray transmission radiography. *Nuclear*

Instruments and Methods in Physics Research, Section A, 563(1):278–281, 2006.

[58] D. Vavřík and P. Soukup. Metal grain structure resolved with table-top micro-tomographic system. *Journal of Instrumentation*, 6(11), 2011.

[59] D. Vavřík, J. Dammer, J. Jakůbek, I. Jeon, O. Jiroušek, M. Kroupa, and P. Zlámal. Advanced X-ray radiography and tomography in several engineering applications. *Nuclear Instruments and Methods in Physics Research, Section A: Accelerators, Spectrometers, Detectors and Associated Equipment*, 633(SUPPL. 1):S152–S155, 2011.

[60] O. Jiroušek, I. Jandejsek, and D. Vavřík. Evaluation of strain field in microstructures using micro-CT and digital volume correlation. *Journal of Instrumentation*, 6(1), 2011.

[61] B. K. Bay, T. S. Smith, D. P. Fyhrie, and M. Saad. Digital volume correlation: Three-dimensional strain mapping using X-ray tomography. *Experimental Mechanics*, 39(3):217–226, 1999.

[62] J.-M. Zhou, L.-H. Qi, and G.-D. Chen. New inverse method for identification of constitutive parameters. *Transactions of Nonferrous Metals Society of China*, 16(1):148 – 152, 2006.

[63] J. Gu, S. Cooreman, A. Smits, S. Bossuyt, H. Sol, D. Lecompte, and J. Vantomme. Full-field optical measurement for material parameter identification with inverse methods. In *High Performance Structures and Materials III*, volume 85, pages 239–248, 04 2006.

[64] B. Chaparro, S. Thuillier, L. Menezes, P. Y. Manach, and J. V. Fernandes. Material parameters identification: Gradient-based, genetic and hybrid optimization algorithms. *Computational Materials Science*, 44:339–346, 12 2008.

[65] P. Zlámal, O. Jiroušek, D. Kytýř, and T. Doktor. Indirect determination of material model parameters for single trabecula based on nanoindentation and three-point bending test. *Acta Technica CSAV (Ceskoslovensk Akademie Ved)*, 58(2):157–171, 2013.

[66] T. Kobayashi. Impact testing. In K. H. J. Buschow, R. W. Cahn, M. C. Flemings, B. Ilschner, E. J. Kramer, S. Mahajan, and P. Veyssière, editors, *Encyclopedia of Materials: Science and Technology*, pages 4027 – 4031. Elsevier, Oxford, 2001.

[67] R. Montanini. Measurement of strain rate sensitivity of aluminium foams for energy dissipation. *International Journal of Mechanical Sciences*, 47(1):26–42, 2005.

[68] V. Králík and J. Němeček. Energy Absorption Of Cellular Foams In High Strain Rate Compression Test. In Grygier, Dominika, editor, *20th Engineering Mechanics*, pages 324–327, 2014.

[69] B. Hopkinson. A method of measuring the pressure in the detonation of high explosives or by the impact of bullets. *Phil. Trans. R. Soc. Lond. A*, 213:437–456, 1914.

[70] H. Kolsky. An investigation of the mechanical properties of materials at very high rates of loading. *Proceedings of the Physical Society. Section B*, 62(11):676–700, nov 1949.

[71] J. Harding, E. O. Wood, and J. D. Campbell. Tensile testing of materials at impact rates of strain. *Journal of Mechanical Engineering Science*, 2(2):88–96, 1960.

[72] W. Goldsmith, J. L. Sackman, and C. Ewerts. Static and dynamic fracture strength of barre granite. *International Journal of Rock Mechanics and Mining Sciences and Geomechanics Abstracts*, 13(11):303 – 309, 1976.

[73] G. T. (Rusty) Gray III. Classic split-Hopkinson pressure bar testing. In *Mechanical Testing and Evaluation*. ASM International, 01 2000.

[74] F. Galina, R. S. Birch, and M. Alves. Design of a split Hopkinson pressure bar. In *17th International Congress of Mechanical Enginering*. ABCM, 2003.

[75] L. Wang, K. Labibes, Z. Azari, and G. Pluvinage. Generalization of split Hopkinson bar technique to use viscoelastic bars. *International Journal of Impact Engineering*, 15(5):669 – 686, 1994.

[76] H. Zhao, G. Gary, and J. R. Klepaczko. On the use of a viscoelastic split Hopkinson pressure bar. *International Journal of Impact Engineering*, 19(4):319 – 330, 1997.

[77] W. Chen, B. Zhang, and M. J. Forrestal. A split Hopkinson bar technique for low-impedance materials. *EXPERIMENTAL MECHANICS*, 39(2):81–85, JUN 1999.

[78] C. Bacon. Separation of waves propagating in an elastic or viscoelastic Hopkinson pressure bar with three-dimensional effects. *International Journal of Impact Engineering*, 22(1):55 – 69, 1999.

[79] T. Fíla. *Mechanical Behavior of Materials under High-strain Rates Investigated by SHPB*. PhD thesis, Czech Technical University in Prague, June 2020. Defended.

[80] O. Jiroušek, T. Doktor, D. Kytýř, P. Zlámal, T. Fíla, P. Koudelka, I. Jandejsek, and D. Vavřík. X-ray and finite element analysis of deformation response of closed-cell metal foam subjected to compressive loading. *Journal of Instrumentation*, 8(2), 2013.

[81] T. Doktor, D. Kytýř, P. Zlamál, T. Fíla, P. Koudelka, and O. Jiroušek. Simulation of a three-point bending test on the isolated cell wall of aluminium foam. *Civil-Comp Proceedings*, 102, 2013.

[82] T. Doktor, D. Kytýř, P. Koudelka, P. Zlámal, T. Fíla, and O. Jiroušek. Determination of elastic-plastic properties of Alporas foam at the cell-wall level using microscale-cantilever bending tests. *Materiali in Tehnologije*, 49(2):203–206, 2015.

[83] T. Doktor, P. Zlámal, T. Fíla, P. Koudelka, D. Kytýř, and O. Jiroušek. Properties of polymer-filled aluminium foams under moderate strain-rate loading conditions. *Materiali in Tehnologije*, 49(4):597–600, 2015.

[84] T. Doktor, P. Zlámal, J. Šleichrt, T. Fíla, and D. Kytýř. Impact Testing of Ordnance Gelatine under Moderate Strain Rate Conditions. In *16TH YOUTH SYMPOSIUM ON EXPERIMENTAL SOLID MECHANICS*, volume 18 of *Acta Polytechnica CTU Proceedings*, pages 44–47, 2018.

[85] T. Doktor, T. Fíla, P. Zlámal, D. Kytýř, and O. Jiroušek. High strain-rate compressive testing of filling materials for inter-penetrating phase composites. In *17th Youth Symposium on Experimental Solid Mechanics*, volume 25 of *Acta Polytechnica CTU Proceedings*, pages 21–24, 2019.

[86] Goodfellow Corp. Product catalogue. available from: www.goodfellow.com/pdf/SHORT3A.pdf.

[87] J. Breeze, M.J. Midwinter, D. Pope, K. Porter, A. E. Hepper, and J. Clasper. Developmental framework to validate future designs of ballistic neck protection. *British Journal of Oral and Maxillofacial Surgery*, 51(1):47–51, 2013.

[88] A. Bracq, G. Haugou, R. Delille, F. Lauro, S. Roth, and O. Mauzac. Experimental study of the strain rate dependence of a synthetic gel for ballistic blunt trauma assessment. *Journal of the Mechanical Behavior of Biomedical Materials*, 72:138 – 147, 2017.

[89] Cumberland Rubber Supply. Ballistic gel, 2018. https://cumberlandrubber.com/gel.html.

[90] Clear Ballistics LLC. 20 % synthetic ballistic gelatin, 2018. https://www.clearballistics.com/shop/20-ballistic-gelatin-ballistics-air-block/.

[91] P. Koudelka, T. Doktor, J. Valach, D. Kytýř, and O. Jiroušek. Effective elastic moduli of closed-cell aluminium foams - Homogenization method. In *11th IMEKO TC15 Youth Symposium on Experimental Solid Mechanics 2012*, pages 244–250, 2012.

[92] T. Fíla, P. Zlámal, P. Koudelka, O. Jiroušek, T. Doktor, and D. Kytýř. Design and use of novel compression device for microtomography under applied load. In J. Naprstek and C. Fischer, editors, *Engineering Mechanics*, pages 60–61, 2012.

[93] T. Doktor, D. Kytýř, P. Zlámal, and O. Jiroušek. Development of volume model of irregular shaped objects for numerical simulations using shape-from-silhouette method. In *11th IMEKO TC15 Youth Symposium on Experimental Solid Mechanics 2012*, pages 88–91, 2012.

[94] G. Bradski. The opencv library. *Dr. Dobb's Journal of Software Tools [online]*, [posted 2008-01-15 19:21:54](article id 2236121):Available from World Wide Web: http://www.drdobbs.com/open–source/the–opencv–library/184404319, 2000.

[95] P. Zlámal. *Microstructural Models for Materials with Porous Structure*. PhD thesis, Czech Technical University in Prague, December 2014. Defended.

[96] V. Králík and J. Němeček. Modelling of macroscopic elastic properties of aluminium foam. In J. Naprstek and C. Fischer, editors, *Engineering Mechanics*, pages 176–177, 2012.

[97] V. Králík and J. Němeček. Two-scale model for prediction of macroscopic elastic properties of aluminium foam. *Chemicke Listy*, 106(SUPPL. 3):s458–s461, 2012.

[98] P. Zlámal, T. Doktor, P. Koudelka, T. Fíla, D. Kytýř, O. Jiroušek, and J. Králík, V.and Němeček. Inspection of local influenced zones in micro-scale aluminium specimens. *Key Engineering Materials*, 606:39–42, 03 2014.

[99] J. Jussila. Preparing ballistic gelatine - review and proposal for a standard method. *Forensic Science International*, 141(2-3):91–98, 2004.

[100] P. Zlámal, O. Jiroušek, and D. Vavřík. A Novel Compression/tension Device for Investigation of Trabecular Bone Failure Using Real-time micro-CT Imaging. In Grygier, Dominika, editor, *7th Youth Symposium on Experimental Solid Mechanics*, pages 91–91, Wroclaw, 2008.

[101] V. Rada, T. Fíla, P. Zlámal, D. Kytýř, and P. Koudelka. Multi-channel control system for in-situ laboratory loading devices. *Acta Polytechnica Proceedings*, 18:15–19, 2018.

[102] T. Fíla, J. Šleichrt, D. Kytýř, I. Kumpová, M. Vopálenský, P. Zlámal, V. Rada, D. Vavřík, P. Koudelka, and S. Senck. Deformation analysis of the spongious sample in simulated physiological conditions based on in-situ compression, 4D computed tomography and fast readout detector. *Journal of Instrumentation*, 13(11), 2018.

[103] D. Kytýř, N. Krcmářová, J. Šleichrt, T. Fíla, P. Koudelka, A. Gantar, and S. Novak. Deformation response of gellan gum based bone scaffold subjected to uniaxial quasi-static loading. *Acta Polytechnica*, 57(1):14–21, 2017.

[104] T. Fíla, P. Zlámal, O. Jiroušek, J. Falta, P. Koudelka, D. Kytýř, T. Doktor, and J. Valach. Impact testing of polymer-filled auxetics using split Hopkinson pressure bar. *Advanced Engineering Materials*, 19(10):1–13, 2017.

[105] J. Falta, P. Zlámal, T. Fíla, and M. Adorna. Labxhpb- shpb/ohpb control and data acquisition software solution. `<http://mech.fd.cvut.cz/software/TDMS_GUI_v2.0.vi>`, 2018.

[106] T. Fíla. Ohpb evaluation toolkit. `<http://mech.fd.cvut.cz/software/ohpb-evaluation-toolkit.zip>`, 2018.

[107] T. Doktor, P. Koudelka, T. Fíla, and O. Jiroušek. Finite element based structural optimization of auxetic structures. *Civil-Comp Proceedings*, 2015.

[108] T. Doktor, T. Fíla, P. Koudelka, D. Kytýř, and O. Jiroušek. Compressive properties of auxetic structures with controlled stiffness of strut joints. In *17th Youth Symposium on Experimental Solid Mechanics*, volume 25 of *Acta Polytechnica CTU Proceedings*, pages 17–20, 2019.

[109] V. S. Deshpande, M. F. Ashby, and N. A. Fleck. Foam topology: Bending versus stretching dominated architectures. *Acta materialia*, 49(6):1035–1040, 2001.

[110] P. Koudelka, O. Jiroušek, T. Fíla, and T. Doktor. Compressive properties of auxetic structures produced by direct 3D printing. *Materiali in Tehnologije*, 50(3):311–317, 2016.

[111] P. Koudelka. *Numerical Modelling of Auxetic Structures*. PhD thesis, Czech Technical University in Prague, September 2020. Submitted.

Appendix A

Candidate's publications related to the dissertation

Papers published in journals with impact factor

1. Jiroušek, O., Doktor, T., Kytýř, D., Zlámal, P., Fíla, T., Koudelka, P., Jandejsek, I., Vavřík, D.: X-ray and finite element analysis of deformation response of closed-cell metal foam subjected to compressive loading, J Instrum, C02012, 2013

   - IF 2014: 1.399; 10 citations

2. Doktor, T., Kytýř, D., Koudelka, P., Zlámal, P., Fíla, T., Jiroušek, O.: Determination of Elastic-plastic Properties of Alporas Foam at Cell-wall Level using Microscale Cantilever Bending Tests, Mater Tehnol, 49(2), 203–206, 2015

   - IF 2016: 0.463; 1 citation

3. Doktor, T., Zlámal, P., Fíla, T., Koudelka, P., Kytýř, D., Jiroušek, O.: Properties of Polymer Filled Aluminium Foam under Moderate Strain Rate Loading, Mater Tehnol, 49(4), 597–600, 2015

   - IF 2016: 0.463; 1 citation
   - awarded by Best paper award at 22nd ICM&T, October 2014

4. Fíla, T., Zlámal, P., Jiroušek, O., Falta, J. , Koudelka, P., Kytýř, D., Doktor, T., Valach, J.: Impact Testing of Polymer-filled Auxetics Using Split Hopkinson Pressure Bar, Adv Eng Mater, 1700076, 2017

   - IF 2018: 2.906; 20 citations

Proceedings papers listed by Scopus and/or Web of Science

1. Doktor, T., Kytýř, D., Zlámal, P., Fíla, T., Koudelka., P., Jiroušek, O.: Simulation of a three-point bending test on the isolated cell wall of aluminium foam. In Proceedings of the 14th International Conference on Civil, Structural and Environmental Engineering Computing, 2013

2. Zlámal, P., Doktor, T., Koudelka, P., Fíla, T., Kytýř, D., Jiroušek, O., Králík, V. and Němeček, J.: Inspection of Local Influenced Zones in Micro-scale Aluminium Specimens, Key Engineering Materials 606, pp. 39–42, 2014

3. Doktor, T., Koudelka., P., Fíla, T., Jiroušek, O.: Finite Element Based Structural Optimization of Auxetic Structures. In Proceedings of the 15th International Conference on Civil, Structural and Environmental Engineering Computing, 2015

4. Doktor, T., Zlámal., P., Šleichrt, J., Fíla, T., Kytýř, D.,Impact Testing of Ordnance Gelatine under Moderate Strain Rate Conditions, Acta Polytechnica Proceedings 18, pp. 44–47, 2018

5. Doktor, T., Fíla, T., Zlámal., P., Kytýř, D., Jiroušek, O.: High Strain-rate Compressive Testing of Filling Materials for Inter-penetrating Phase Composites, Acta Polytechnica Proceeding 25, pp. 21–24, 2019

6. Doktor, T., Fíla, T., Koudelka., P., Kytýř, D., Jiroušek, O.: Compressive Properties of Auxetic Structures with Controlled Stiffness of Strut Joints, Acta Polytechnica Proceedings 25, pp. 17–20, 2019

Candidate's publication and citation metrics

- Number of records in Web of Science and/or Scopus is 57.
- Number of citations in Web of Science and/or Scopus is 112.*
- Hirsch index is 5.

*In the presented citation metrics, direct and indirect self-citations are excluded.